

# Antiperovskites with Exceptional Functionalities

Yonggang Wang, Hao Zhang, Jinlong Zhu, Xujie Lü, Shuai Li, Ruqiang Zou,\*  
and Yusheng Zhao\*

HPSTAR  
1005-2020

ABX<sub>3</sub> perovskites, as the largest family of crystalline materials, have attracted tremendous research interest worldwide due to their versatile multifunctionalities and the intriguing scientific principles underlying them. Their counterparts, antiperovskites (X<sub>3</sub>BA), are actually electronically inverted perovskite derivatives, but they are not an ignorable family of functional materials. In fact, inheriting the flexible structural features of perovskites while being rich in cations at X sites, antiperovskites exhibit a diverse array of unconventional physical and chemical properties. However, rather less attention has been paid to these “inverse” analogs, and therefore, a comprehensive review is urgently needed to arouse general concern. Recent advances in novel antiperovskite materials and their exceptional functionalities are summarized, including superionic conductivity, superconductivity, giant magnetoresistance, negative thermal expansion, luminescence, and electrochemical energy conversion. In particular, considering the feasibility of the perovskite structure, a universal strategy for enhancing the performance of or generating new phenomena in antiperovskites is discussed from the perspective of solid-state chemistry. With more research enthusiasm, antiperovskites are highly anticipated to become a rising star family of functional materials.

physics owing to their numerous significant properties supporting the operation of the modern world, such as magnetism, ferroelectricity, multiferroicity, superconductivity, and the ability to act as catalysts and battery materials.<sup>[2]</sup> Very recently, the discovery of organic–inorganic hybrid perovskites applied as photovoltaic materials has once again greatly stimulated the research field of perovskites.<sup>[3–6]</sup> Antiperovskites can also be described by the formula ABX<sub>3</sub>, but electronically inverted (X is a cation, and A and B are anions, accordingly written as X<sub>3</sub>BA).<sup>[7–12]</sup> From the viewpoint of structure chemistry, antiperovskites should share the advantages of the perovskite-type structure with traditional perovskites, accommodating diverse elements to form a large family of functional materials. Indeed, antiperovskites have shown various interesting properties, such as magnetism, ionic conductivity, superconductivity, negative thermal expansion, the ability to act as photoluminescence host materials,

## 1. Introduction

Perovskites, named after the Russian mineralogist L. A. Perovski in 1839,<sup>[1]</sup> comprise materials with the general formula ABX<sub>3</sub>, a deceptively simple structure with a built-in potential for structural complexity and surprising properties. Perovskites have always been a major player in solid-state chemistry and

and other utilities. These exhilarating findings can be highly expected to prompt a new round of development of functional antiperovskites. We can also ask how can we structurally design antiperovskites similar to perovskites to improve their performance or realize unexpected phenomena?

In the antiperovskite formula X<sub>3</sub>BA, X is a cation, and A and B are different-sized anions. The ideal antiperovskite structure with cubic space group *Pm-3m* (*O<sub>h</sub>*) is depicted in **Figure 1**, where the B anions are located in the center of sixfold coordinated octahedra and the A anions are 12-fold coordinated with the X cations. The 3D skeleton of the structure is formed by corner-sharing BX<sub>6</sub> octahedra. Compared to traditional perovskites, cations take the place of anions in the octahedra, and these abundant X site cations endow antiperovskites with unconventional physical and chemical properties related to d-spin states/the band structure or ion transport. Figure 1 also shows the elemental constituents of thus far known antiperovskites. Usually, monovalent or divalent cations are located at the X site, and small anions are located at the B site. Notably, some transition metals can serve as both A and X elements in different cases depending on the relative ionic radius and electronegativity, which has rarely been observed in traditional perovskites. At first glance, antiperovskites appear to already comprise nearly half of the elements in the periodic table. In fact, no more than ten elements occur frequently in the reported

Prof. Y. Wang, Dr. H. Zhang, Prof. R. Zou  
Beijing Key Lab of Advanced Battery Materials  
Department of Materials Science and Engineering  
College of Engineering  
Peking University  
Beijing 100871, China  
E-mail: rzou@pku.edu.cn

Prof. Y. Wang, Prof. J. Zhu, Prof. X. Lü  
Center for High Pressure Science and Technology Advanced Research  
(HPSTAR)  
Beijing 100094, China

Dr. S. Li, Prof. Y. Zhao  
Academy for Advanced Interdisciplinary Studies  
Southern University of Science and Technology  
Shenzhen 518055, China  
E-mail: zhaoy@sustech.edu.cn

 The ORCID identification number(s) for the author(s) of this article can be found under <https://doi.org/10.1002/adma.201905007>.

DOI: 10.1002/adma.201905007

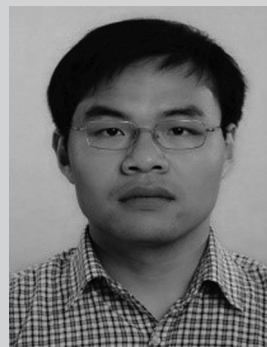
antiperovskites. The number of antiperovskite compounds is still very limited compared with the great possibilities shown in the elemental periodic table. Studies on antiperovskites are still rare, with no more than fifty papers published annually, due to the relatively few quantitatively discovered antiperovskites. The concept “anti” is not widely acknowledged, and sometimes, the newly discovered antiperovskites are simply treated as intermetallic compounds or dual-metal nitrides/carbides, unaware of their unique structure. Nevertheless, the importance of antiperovskites is far beyond our expectations.

Herein, we review recent explorations of antiperovskite-type materials, focusing particularly on their crystal structure features and emerging physical properties and functionalities. We present a general background on the current research status of antiperovskites and their potential to be a large family of functional materials. Synthesis strategies for bulk and nano-sized materials are also discussed. Rather than trying to cover the entire field, we focus on the crystal structure features and emerging functionalities of antiperovskites. We also discuss structural manipulation methods for improving their performance in several fields. We conclude with an overview of the structure–property relationships of antiperovskite-type materials, a perspective on the future exploration of new antiperovskites, and their potential for various practical applications.

## 2. Structural Features of Antiperovskites

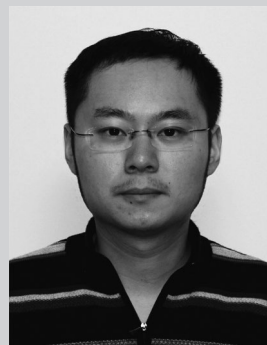
The tolerance factor ( $t$ ) was introduced for perovskites to deduce their crystallographic stability and probable structural symmetry, defined by the equation  $t = (r_A + r_X) / [\sqrt{2}(r_B + r_X)]$ , where  $r_A$ ,  $r_B$ , and  $r_X$  are the ionic radii of the corresponding ions. The cubic structure likely exists when  $t$  lies in the range of 0.85–1.0, and lower  $t$  values give tetragonal or orthorhombic structures or other structures with even lower crystallographic symmetry. In a cubic ionic antiperovskite  $X_3BA$ , the relationship between the ionic radii can also be obtained by  $r_A + r_X = \sqrt{2}(r_B + r_X)$ . In practice, most antiperovskites are built up of p-elements (such as Al, Ga, and Ge) preferring covalent bonds and d- or f-elements (such as V, Cr, Mn, and Ni) preferring metallic bonds. In such cases, using the tolerance factor to determine the existence of a proposed antiperovskite or predict the crystallographic symmetry is difficult. By comprehensively considering  $t$ ,  $R_A/R_B$  and the types of interatomic bonds, Beznosikov<sup>[12]</sup> tried to predict metallic nitrides with an antiperovskite-type structure. However, the practicality and effectiveness of the prediction method have not yet been verified. The cubic structure is still retained in metallic  $X_3BA$  compounds even though the abovementioned equation is not exactly obeyed, deviating from the ideal situation.

Deficiencies or nonstoichiometry are frequently observed in traditional perovskites, producing interesting structure types and significant physical properties. Well-known examples are oxygen-deficient brownmillerite  $\text{CaFeO}_{2.5}$  and  $\text{LaNiO}_{2.5}$  and the  $\text{ReO}_3$ -type compounds (A site vacant). Likewise, deficient structures are also expected to lead to emerging properties in antiperovskites. Taking the antiperovskite  $\text{Hg}_3\text{Q}_2\text{X}_2$  ( $\text{Q} = \text{S}, \text{Se}, \text{Te}; \text{X} = \text{Cl}, \text{Br}, \text{I}$ ) as an example (Figure 2b),<sup>[13–18]</sup> the defect structure is derived from the stoichiometric  $\text{BaTiO}_3$ -type



**Yonggang Wang** received his B.S. degree (2005) from Nankai University and his Ph.D. degree (2010) in physical chemistry from TIPC, Chinese Academy of Sciences. He joined the group of Prof. Jianhua Lin at Peking University as a postdoctoral fellow (2010–2013) and then joined the group of

Prof. Yusheng Zhao at HiPSEC, University of Nevada Las Vegas as a postdoctoral fellow. He became a professor at the Center for High Pressure Science and Technology Advanced Research (HPSTAR, Beijing) in September 2017. His research interests focus on antiperovskite electrolytes, structural design of new functional materials, and exploration of pressure-responsive switching materials.



**Hao Zhang** received his B.S. degree (2011) in material science from China University of Geosciences and his Ph.D. degree (2016) in inorganic chemistry from the College of Chemistry, Peking University. He then joined the group of Prof. Ruqiang Zou at the College of Engineering, Peking University as a postdoctoral fellow in

2016. His research interests focus on the exploration of perovskite and antiperovskite materials for electrochemical energy storage.



**Ruqiang Zou** is currently a Professor of Materials Science and Engineering, Peking University, China. He received his Ph.D. in engineering in 2008 from Kobe University and AIST, Japan. He held a JSPS Younger Scientist during his doctoral course and a Director's Postdoc Fellow at Los Alamos National Laboratory from 2008 to

2010. His research interests focus on the controllable preparation and application of hierarchically porous functional materials for energy and environmental application.

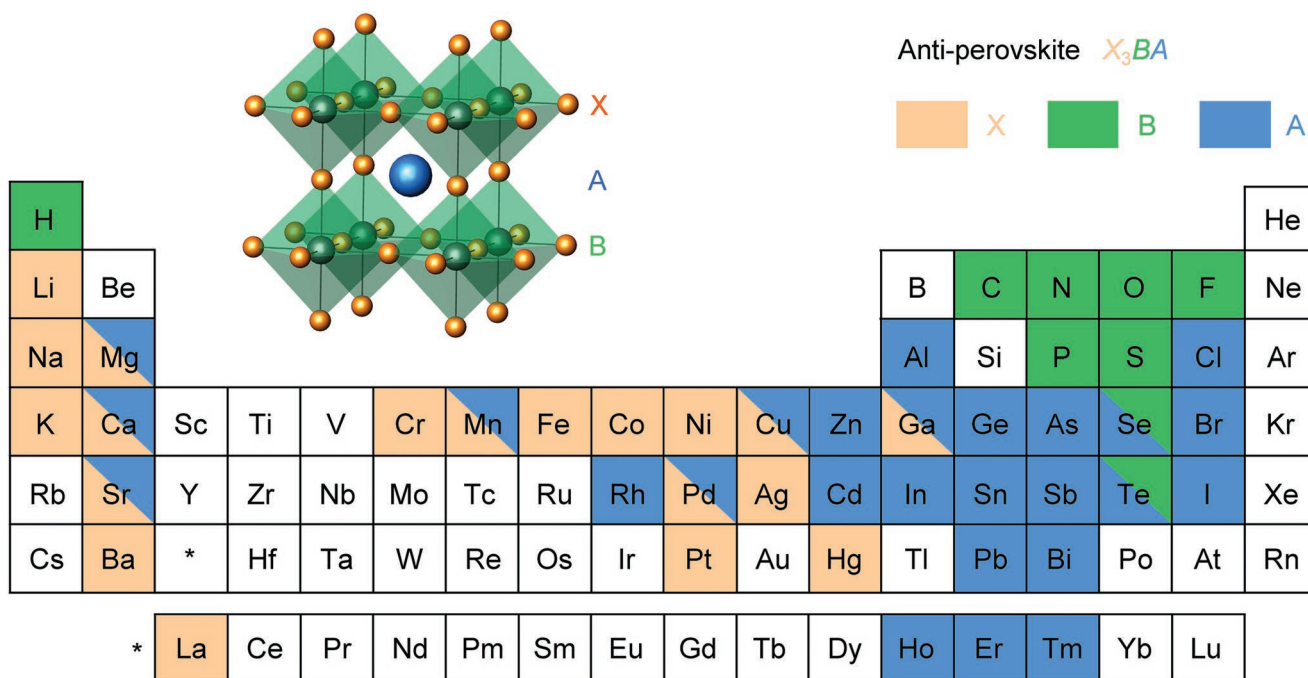


**Figure 1.** Crystal structure of a cubic antiperovskite and elemental constituents of thus far known antiperovskites  $X_3BA$ . The X site elements are shown in brown. The B and A site elements are shown in green and blue, respectively. Note that some elements can occupy two distinct positions in the antiperovskite structure in different compounds.

$X[QHg_3]$ .<sup>[19]</sup> The  $[QHg_3]^{4+}$  pyramids can be considered incomplete  $[QHg_3\Box_3]^{4+}$  octahedra ( $\Box$  denotes a vacancy), and the  $Hg_3Q_2X_2$  compounds can be described as defective antiperovskites with the idealized formula “ $Hg_6Q_2X_2$ ” but with 50% of the Hg atoms missing to produce  $Hg_3\Box_3Q_2X_2$ . The determining factor for the dimensionality of the  $Hg_3Q_2X_2$  lattice is the relative connectivity of the  $[QHg_3]^{4+}$  pyramids. Depending on Q, the ordering of the Hg vacancies varies, yielding a rich family

of distinct crystal structures ranging from 3D to 0D. The structural evolution of the  $[Q_2Hg_3]$  motifs is also considered essential for determining the physical properties of the  $Hg_3Q_2X_2$  compounds. All three  $Hg_3Q_2I_2$  materials demonstrate suitable optical, suitable electrical and good mechanical properties required for radiation detection at room temperature.  $Fe_2SeO$  is another defective antiperovskite with 1/3 of the  $Fe^{2+}$  cations missing in the structure.<sup>[20]</sup> As a transition-metal-dominated

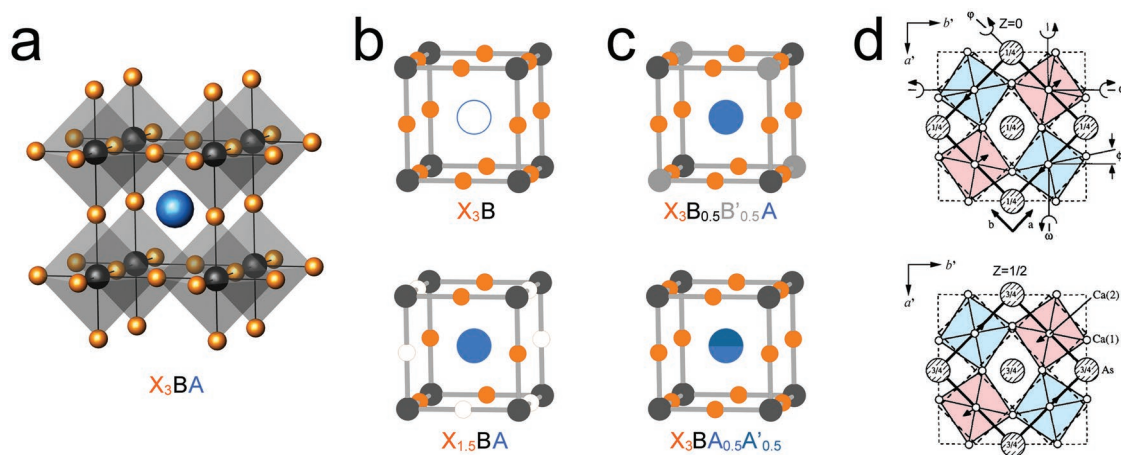


**Figure 2.** Representation of antiperovskite-type crystal structures. a) Crystal structure of a stoichiometric antiperovskite  $X_3BA$  with cubic space group  $Pm-3m$ . b) Representative deficient antiperovskite structures with the formulas  $X_3B$  and  $X_{1.5}BA$ . c) Representative double antiperovskite structures with elemental mixing at the B and A sites. d) Observed tilt of  $Ca_3AsN$  as a representative tilted antiperovskite structure. The dotted lines are the doubled ideal cubic cell containing eight nitrogen-centered calcium octahedra. The solid lines outline the distorted structure, and the unit cell is drawn with the bold solid lines. (Ca: small open circles, As: large hatched circles, N: not shown.) The tilt angles and directions of the octahedra about the  $c$ -,  $a'$ - (or  $b'$ -), and  $b$ -axes are indicated by the arrowed semicircles and are labeled  $\phi$ ,  $\omega$ , and  $\varphi$ , respectively. Reproduced with permission.<sup>[24]</sup> Copyright 1992, Elsevier.

deficient antiperovskite, it shows great potential to be adopted as a cathode material.<sup>[21]</sup> Following this line of thought, numerous double antiperovskites can also be made with formulas such as  $X_3BA_{0.5}A'_{0.5}$  and  $X_3B_{0.5}B'_{0.5}A$  (Figure 2c).

Although ideal antiperovskites adopt a cubic geometry, in real compounds, they are often pseudocubic or distorted into lower symmetries. While antiperovskites show fewer distorted examples than perovskites, structural distortions will certainly affect their physical properties. Perovskite distortions can always be broken down into several simple components: a) tilting of the octahedra, b) distortion of the octahedra, and c) displacement of the cations. Among them, tilting of the octahedra often dominates the overall crystal structure, and a total of 23 possible space groups exist due to the rotation of the rigid octahedra.<sup>[22,23]</sup> Figure 2d shows the crystal structure of  $Ca_3AsN$  with a distorted antiperovskite structure, in which an orthorhombic unit cell ( $b \sim \sqrt{2}a'$ ,  $c \sim 2a'$ ) is adopted.<sup>[24]</sup> Tilting of the  $Ca_6N$  octahedra results in 6 short and 6 long bond distances of the 12-fold coordinated As atoms, which belongs to the tilt system  $a^-a^-c^+$  according to Glazer's classification of distortion. Distortions have also been observed in  $Cr_3AsN$ ,<sup>[25]</sup> with  $a^0b^0c^-$  type rotations of  $Cr_6N$  and  $Mn_3NA$  ( $A = Cu, Ga, Ge, As, Sb$ ), which exhibits phase transitions to lower symmetry due to rotations of the  $Mn_6N$  octahedra.<sup>[26]</sup>

One of the most important structural features of an antiperovskite  $X_3BA$  is the unusual coordination environment of cation X (i.e., the X–X distance and linear twofold coordination versus sixfold coordination in perovskites), which plays a crucial role in magnetic interactions or the crystal field strength. Another noteworthy structural feature of antiperovskites is that they are X-rich. Physical properties, such as the magnetism and ionic conductivity, are strongly related to the X-rich feature of antiperovskites. The discovery of superionic conductivity in Li-rich antiperovskites (LiRAPs) was inspired by the high-temperature superionic conductivity of the  $NaMgF_3$  and  $(K,Na)MgF_3$  perovskites.<sup>[27]</sup> Thus, the “electronically inverted” antiperovskite  $Li_3OA$  ( $A = Cl, Br, I$ ) preserves the perovskite-type structure and allows  $Li^+$  superionic conductivity similar to the  $F^-$  superionic conductivity in  $NaMgF_3$ , benefiting from the Li-rich nature. Such newly designed antiperovskite crystalline solids are lithium-rich (60 at% Li) and lightweight. The X-rich structural feature also leads to 3D migration paths of the  $X^+$  ions that favor high ionic conductivity. For magnetic antiperovskites, the magnetic exchange within the transition-metal-rich topology is obviously distinct compared to that embedded in nonmagnetic skeletons, and a metallic ground state is expected.

### 3. General Strategies for Synthesizing Antiperovskite Compounds

Generally, powder samples of most antiperovskite compounds can be synthesized by the direct solid-state sintering method. Protective atmospheres are necessary for air- or moisture-sensitive materials. For example, ionic conductors  $A_3OX$  ( $A = Li, Na, Ag; X = Cl, Br, I$ ) have been fabricated starting from  $A_2O$  oxides and  $AX$  with a molar ratio of 1:1. To avoid absorption of moisture, all the mixing and pressing processes should be performed in an inert gas-filled glove box. For the syntheses of

antiperovskite nitrides  $X_3BN$  ( $X = Ca, Sr, Ba, Mn, Ni, Co; B$  is a group-IV or group-V element), nitrogen-excess reagents may be adopted to release redundant nitrogen gas during high-temperature sintering. A family of alkali-metal-rich antiperovskites  $Ca_3MN$  ( $M = P, As, Sb, Bi, Ge, Sn, Pb$ ) was synthesized using this method.<sup>[28]</sup> Chemical manipulations, such as elemental doping and deficiencies, can be achieved by simply varying the ratio of the starting materials.

Chemical nitridation of intermetallic or oxide precursors is another frequently used method to obtain ternary antiperovskite nitrides. In the case of iron-containing antiperovskite nitrides, avoiding the formation of stable binary impurities is always difficult due to their lower formation energies. In this situation, a two-step ammonolysis method combining a high-temperature (1000–1300 °C) sintering step and a low-temperature (500–600 °C) nitriding reaction was proposed to produce  $Fe_3BN$  ( $B = Rh, Ga, Al$ ) with improved phase purity.<sup>[29]</sup>  $NH_3$  was used as the ammonolysis agent. Brady et al. demonstrated that intermetallic  $Cr_3Pt$  alloys could be used as precursors to form  $Cr_3PtN$  antiperovskites in a  $N_2$  atmosphere.<sup>[30]</sup> A higher reaction temperature (i.e.,  $\approx 1000$  °C) is needed for  $N_2$  with lower reactivity. Metal oxides can also be used as metal sources in an ammonolysis synthesis process due to the high reactivity of  $NH_3$  in substituting the oxygen atoms in the raw materials. Ternary antiperovskite nitrides  $X_3InN$  ( $X = Ni, Co$ ) were reported to be successfully fabricated from  $In_2O_3$  and  $Ni/Co$  powders under  $NH_3$  flow at 600 °C.<sup>[31]</sup> Recently, Wang's group also reported the successful preparation of thin films of antiperovskites  $Mn_3CuN$  and  $Mn_3NiN$  by using dc reactive magnetron sputtering with either separated  $Mn/Cu$  targets or a  $Mn-Ni$  alloy target in an  $Ar/N_2$  atmosphere.<sup>[32,33]</sup> Moreover, a single crystal of antiperovskites (e.g.,  $Ni_3MgC$ ) can be grown from the self-flux method with the aid of a high pressure (4.25 GPa).<sup>[34]</sup>

Antiperovskites with high porosity and a hybrid core-shell architecture are requested to realize advanced electrocatalysts with both high catalytic activity and robust stability. Recently, an antiperovskite-based hybrid with a porous conductive  $Ni_{3-y}Cu_{1-x}N$  core and an amorphous  $FeNiCu$  (oxy)hydroxide shell was developed as a promising water oxidation electrocatalyst.<sup>[35]</sup> For the fabrication procedure of the  $p-Ni_{3-y}Cu_{1-x}N/FeNiCu$  hybrid, the Cu-excess antiperovskite  $Ni_3CuN+Cu$  was first synthesized from a mixture of  $Cu$  and  $Ni$  powders through solid-gas reactions. Excess  $Cu$  was intentionally introduced to serve as a sacrificial template for the creation of rich pores during the subsequent etching process. Then, the as-obtained polycrystalline was etched by an  $Fe^{3+}$  aqueous solution to form an  $FeNiCu$  (oxy)hydroxide colloid and deposited on the surface of the antiperovskite phase. The detailed reaction equations include 1)  $Cu + 2Fe^{3+} \rightarrow Cu^{2+} + 2Fe^{2+}$ , 2)  $Ni + 2Fe^{3+} \rightarrow Ni^{2+} + 2Fe^{2+}$ , and 3)  $Fe^{3+} + Ni^{2+} + Cu^{2+} + OH^- \rightarrow FeNiCu$  (oxy)hydroxide +  $H^+$ . Finally, a  $p-Ni_{3-y}Cu_{1-x}N/FeNiCu$  core-shell hybrid was fabricated with highly efficient and robust oxygen evolution reaction (OER) performance, outperforming the benchmark  $IrO_2$  catalyst in several aspects.

Traditional high-temperature synthetic methods can lead to various thermodynamically stable antiperovskites for studies of their intrinsic physical properties. Low-temperature soft chemical methods, such as ammonolysis, have great potential to generate metastable antiperovskites or those with a unique

stoichiometry. Additionally, modern construction strategies for nanosized materials can also be widely applied in the fabrication of antiperovskites with greatly improved performances. One has every reason to anticipate the rapid development of antiperovskites as advanced functional materials.

## 4. Emerging Functionalities of Antiperovskites

In the introduction, we discussed in general terms how various intriguing functionalities of perovskite oxides can be obtained from a wide range of perovskite-type structures. Although less frequently observed, several intriguing phenomena have also been reported in antiperovskite materials. Here, we highlight the physical properties of antiperovskites, including their superionic conductivity, magnetism, negative thermal expansion, superconductivity, and ability to act as phosphor hosts and electrocatalysts. Notably, the flexibility of the antiperovskite structure enables various chemical manipulations toward greatly enhanced performance. In each part, we will discuss the syntheses of perovskite compounds if necessary. Personal perspectives and emerging structural design strategies toward antiperovskites with better performance are also provided.

### 4.1. Antiperovskites as Advanced Battery Materials

The urgent energy demands of the modern industrialized world have triggered much research interest in developing efficient energy storage devices, especially lightweight  $\text{Li}^+/\text{Na}^+$  batteries with a high energy density.<sup>[36]</sup> The primary strategy for realizing this aim is to develop advanced electrode materials with a high capacity and a large voltage window. Among various materials, Li metal anode materials render an ultrahigh theoretical specific capacity ( $3860 \text{ mA h g}^{-1}$ ) and the most negative electrochemical potential ( $-3.040 \text{ V}$  vs reversible hydrogen electrode (RHE)). A battery cell with a Li metal anode is therefore expected to power

electronic products for a long time while remaining lightweight. However, to achieve this vision, the flammability and easy-leak feature of the conventional electrolyte must first be overcome. A safe solid-state electrolyte (SSE) has therefore been proposed as a replacement, and the most attractive property is that the SSE would not only address the safety concerns due to inflammability but also improve the energy density when it is of ultrathin thickness. Batteries supported by SSEs are on the cusp of being a commercial technology.<sup>[37]</sup>

However, SSEs still encounter formidable challenges, including surface contact, Li dendrite growth, stability, ionic conductivity, etc.<sup>[38]</sup> Here, we mainly discuss the ionic conductivity of the antiperovskite family. Solid electrolytes are expected to have an ionic conductivity of  $\sigma \approx 10^{-2} \text{ S cm}^{-1}$ , as high as an ionic liquid at room temperature; however, without optimization by material engineering, few of these electrolytes can approach such a high level. Considerable research has focused on seven classes of inorganic SSEs, including LISICON-like materials, argyrodites, garnets, NASICON-like materials, lithium nitrides, lithium hydrides, perovskites, and lithium halides.<sup>[39–49]</sup>

A pioneering work developed the LiRAP  $\text{Li}_3\text{OA}$  ( $A = \text{Cl}, \text{Br}$ ) as a superionic solid electrolyte,<sup>[27]</sup> achieving a Li ionic conductivity as high as  $1.94 \times 10^{-3} \text{ S cm}^{-1}$  in  $\text{Li}_3\text{OCl}_{0.5}\text{Br}_{0.5}$ . Importantly, the performance of LiRAPs can be improved via various structural design strategies. **Figure 3** presents the structural design strategies for antiperovskites toward enhanced ionic conductivity, such as A site mixing to generate lattice mismatch, X site doping and “XA” depletion to generate vacancies, and A site clustering to induce an order–disorder transition. Notably, all these methods aiming at superionic conductivities are simultaneously applicable to one antiperovskite. In  $\text{Li}_3\text{OA}$ , halogen mixing ( $\text{Cl}_{1-z}\text{Br}_z$ ) can push the tolerance factor from 0.85 for pure  $\text{Li}_3\text{OCl}$  to 0.91 for pure  $\text{Li}_3\text{OBr}$ , which represents a less pseudocubic lattice distortion that can promote a displacive structural phase transition via phonon softening. Such structural manipulation could promote

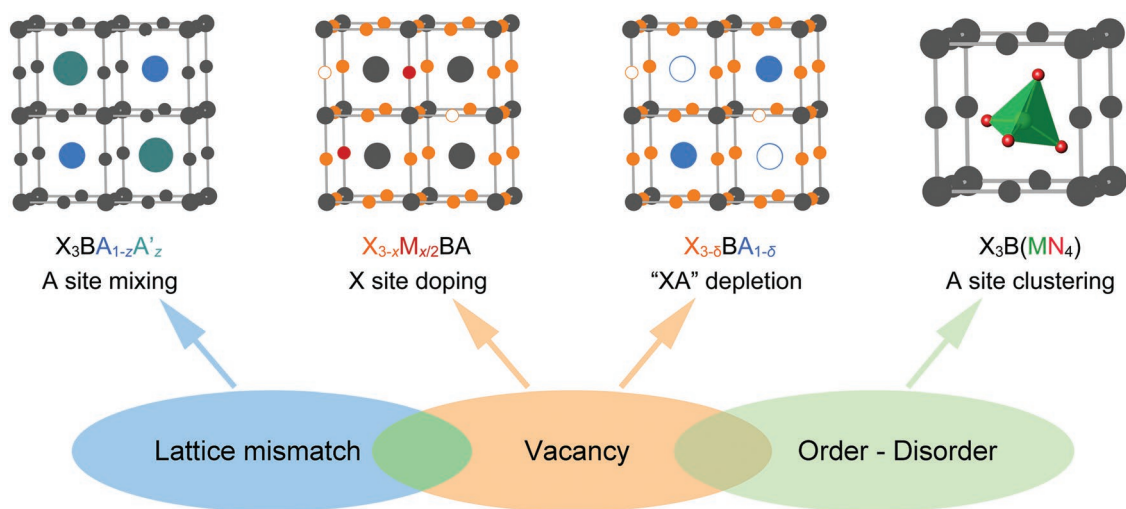


**Figure 3.** Structural design strategies for antiperovskites toward enhanced ionic conductivity. The antiperovskite structures illustrate the effects of A site mixing to generate lattice mismatch, X site doping and “XA” depletion to generate vacancies, and A site clustering to induce an order–disorder transition. Notably, the four methods are simultaneously applicable to one antiperovskite.

superionic conduction via Frenkel interstitial transport, and the mixed  $\text{Li}_3\text{OCl}_{0.5}\text{Br}_{0.5}$  shows higher ionic conductivity and lower activation energy than pure  $\text{Li}_3\text{OCl}$ . Composition optimization of  $\text{Li}_3\text{OCl}_{1-x}\text{Br}_x$  shows that an even higher ionic conductivity can be achieved in  $\text{Li}_3\text{OCl}_{1-x}\text{Br}_x$  within  $0.235 \leq x \leq 0.395$ .<sup>[50]</sup> Similarly, divalent cation doping ( $\text{Li}_{3-x}\text{M}_{x/2}\text{OA}_{1-z}\text{A}'_z$ ) can increase the concentration of electronic vacancies at the Li sites to promote neighboring ion hopping via the Schottky route.<sup>[51]</sup> Moreover, introducing vacancies at both the cation and anion sites ( $\text{Li}_{3-\delta}\text{O}(\text{A}_{1-z}\text{A}'_z)_{1-\delta}$ ) can produce lattice defects/channels for higher ionic conduction. The highest ionic conductivity reaches  $\sigma > 10^{-3} \text{ S cm}^{-1}$  in  $\text{Li}_3\text{OCl}_{0.5}\text{Br}_{0.5}$  at room temperature, comparable to that of the best  $\text{Li}^+$  solid electrolyte  $\text{Li}_{10}\text{GeP}_2\text{S}_{12}$  ( $1.2 \times 10^{-3} \text{ S cm}^{-1}$  at room temperature).<sup>[52]</sup>

A pulsed laser deposition (PLD) method was used to fabricate a  $\text{Li}_3\text{OCl}$  film with an ionic conductivity of  $0.9 \times 10^{-5} \text{ S cm}^{-1}$  at room temperature.<sup>[53]</sup> Subsequent studies improved the room temperature ionic conductivity to  $2.0 \times 10^{-4} \text{ S cm}^{-1}$ <sup>[54]</sup> before the feasibility of using the optimized  $\text{Li}_3\text{OCl}$  film in a real battery  $\text{LiCoO}_2|\text{Li}_3\text{OCl}|\text{C}$  was demonstrated. The battery has an initial discharge capacity of  $120 \text{ mA h g}^{-1}$  and a discharge efficiency of 95% after the second cycle. The  $\text{Li}_3\text{OCl}$ -based glassy electrolyte with divalent cation doping exhibits an extremely high ionic conductivity of  $25 \text{ mS cm}^{-1}$  at room temperature,<sup>[55]</sup> above those of all other lithium superionic conductors, and is chemically stable with respect to the Li metal.

The idea of LiRAPs can also be extended to the design of Na batteries with the development of a series of Na-rich antiperovskites (NaRAPs)<sup>[56,57]</sup> and intergrowth NaRAPs:  $\text{Na}_4\text{OI}_2$  and  $\text{Na}_3\text{SO}_4\text{F}$ .<sup>[58,59]</sup> Larger  $\text{Na}^+$  ions are better for stabilizing the antiperovskite structure, and hence, more NaRAPs are expected. In the solid solution  $\text{Na}_3\text{OX}$  ( $\text{X} = \text{Cl}, \text{Br}, \text{I}$ ), lattice mismatch and nonequivalent-doping strategies have been successfully adopted to promote the performance.<sup>[60]</sup> The optimized  $\text{Na}_{2.9}\text{Sr}_{0.05}\text{OBr}_{0.6}\text{I}_{0.4}$  exhibits a conductivity beyond  $10^{-2} \text{ S cm}^{-1}$  when approaching the melting point. However, the design of intergrowth antiperovskite  $\text{Na}_4\text{OI}_2$  reveals an anisotropic sodium transport route.<sup>[61]</sup> Notably, since the alkali-metal-rich antiperovskites (both Li-rich and Na-rich) are very sensitive to moisture, researchers usually struggle with high phase purity and stable performance problems. Phase-pure powders of  $\text{Na}_3\text{OX}$  can be synthesized using sodium metal as the raw material according to the following reaction equation:  $\text{Na} + \text{NaOH} + \text{NaX} \rightarrow \text{Na}_3\text{OX} + 1/2 \text{ H}_2\uparrow$ .<sup>[62]</sup> The sodium metal serves as not only one of the raw materials inside but also the scavenger of trace moisture.

Recent experimental and theoretical studies also focused on the improvement of LiRAPs via A site clustering to induce an order-disorder transition. Substitution of  $\text{F}^-$  for  $\text{OH}^-$  in  $\text{Li}_2(\text{OH})_{0.9}\text{F}_{0.1}\text{Cl}$  could stabilize the cubic phase of  $\text{Li}_2\text{OHCl}$  to decrease the activation energy for  $\text{Li}^+$  transport.<sup>[63]</sup> Moreover, this fluorine-doped LiRAP is stable upon contact with metallic Li and has an energy window extending to 9 V versus  $\text{Li}^+/\text{Li}$ . Theoretical calculations revealed the possibility of including clusters in LiRAPs for enhanced ionic conductivity, such as  $\text{Li}_3\text{OCl}_{0.5}(\text{BH}_4)_{0.5}$ ,  $\text{Li}_3\text{O}(\text{BH}_4)$ ,  $\text{Li}_3\text{S}(\text{BF}_4)_{0.5}\text{Cl}_{0.5}$ , and  $\text{Li}_3\text{SBF}_4$ .<sup>[64,65]</sup> The ionic conductivity of  $\text{Li}_3\text{OCl}_{0.5}(\text{BH}_4)_{0.5}$  can reach  $0.21 \times 10^{-3} \text{ S cm}^{-1}$  at room temperature, with an activation energy of 0.299 eV, while in  $\text{Li}_3\text{S}(\text{BF}_4)_{0.5}\text{Cl}_{0.5}$ , the value can even

reach  $10^{-1} \text{ S cm}^{-1}$ , with a lower activation energy of 0.176 eV. The high  $\text{Li}^+$  conductivity of these materials was ascribed to the thermal excitation of the quasi-rigid unit modes of the  $\text{BH}_4^-$  cluster and the exceptionally large channel size created by mixing the large cluster ions together with the elementary ions. This idea can also be extended to design novel clusters in NaRAPs, such as  $\text{Na}_3\text{OA}$  ( $\text{A} = \text{BH}_4, \text{NO}_3, \text{and CN}$ ).<sup>[65]</sup>

Starting from the discovery of the cation-deficient antiperovskite  $\text{Fe}_2\text{OSe}$ ,<sup>[20]</sup>  $(\text{Li}_2\text{Fe})\text{OCh}$  ( $\text{Ch} = \text{S}, \text{Se}, \text{Te}$ ) were proposed as a new family of cathode materials,<sup>[21]</sup> where  $\text{Li}^+$  can be inserted into the cation vacancy sites and be randomly distributed with Fe ions.  $(\text{Li}_2\text{Fe})\text{OCh}$  adopt a cubic antiperovskite structure for  $\text{Ch} = \text{S}, \text{Se}$  and a 4H distorted antiperovskite structure for  $\text{Ch} = \text{Te}$ . The general reaction for charging/discharging is  $(\text{Li}_2\text{Fe})\text{SeO} + n\text{C}(\text{graphite}) \rightarrow (\text{Li}_{2-x}\text{Fe})\text{SeO} + \text{Li}_x\text{C}_n$ , with the average oxidation state of Fe changing from  $2^+$  to  $(2+x)^+$ .  $(\text{Li}_2\text{Fe})\text{ChO}$  ( $\text{Ch} = \text{S}, \text{Se}$ ) were tested as cathode materials against graphite anodes, and they performed similarly, with outstanding specific charge capacities of  $60 \text{ mA h g}^{-1}$  at a very high charge rate ( $270 \text{ mA g}^{-1}$ , 80 cycles) and  $120 \text{ mA h g}^{-1}$  at a charge rate of  $30 \text{ mA g}^{-1}$ , which is comparable to the experimental value of  $160 \text{ mA h g}^{-1}$  for  $\text{Li}_{1-x}\text{CoO}_2$ .<sup>[66]</sup> This antiperovskite cathode material has lower pristine oxidation states of  $\text{Fe}^{2+}$  compared to  $\text{TM}^{3+}$  in delafossites  $\text{LiTMO}_2$  ( $\text{TM} = \text{Co}, \text{Mn}, \text{Ni}$ ), which can lower the working potential window and stabilize standard battery constituents during the charge/discharge processes, and only exhibits a faint capacity loss during 80 charge/discharge cycles at high rates.

Generally,  $\text{Li}^+/\text{Na}^+$  antiperovskites exhibit promising intrinsic high ionic conductivity, which can be further optimized through structural design and chemical doping. The good stability and low surface resistance when they contact Li metal anodes are two other advantages for commercial applications. However, their high sensitivity to moisture and low potential window are two drawbacks that need to be overcome. Large-scale industrial fabrication with low cost remains to be further investigated.

## 4.2. Magnetism and Magnetoresistance in Antiperovskites

Magnetic perovskite oxides  $\text{ABO}_3$  have been widely used in modern devices, such as storage devices and those involving magnetocaloric effects and magnetoresistivity.<sup>[67-71]</sup> Magnetic antiperovskites  $\text{M}_3\text{M}'\text{X}$  ( $\text{M} = \text{Mn}, \text{Fe}, \text{etc.}; \text{M}' = \text{Ga}, \text{Al}, \text{Zn}, \text{In}, \text{Sn}, \text{etc.}; \text{X} = \text{N}, \text{C}$ ) have also been frequently studied as a new class of promising magnetic materials. Among them, Mn-based magnetic antiperovskites are the most attractive due to their recently reported giant magnetoresistance (GMR),<sup>[72,73]</sup> large magnetocaloric effect (MCE),<sup>[74,75]</sup> and giant magnetostriction (MS).<sup>[76-78]</sup> Moreover, these  $\text{Mn}_3\text{M}'\text{X}$  antiperovskites are metallic, indicating good electric and thermal conductivity and mechanical properties.<sup>[79]</sup>

$\text{Mn}_3\text{GaC}$  is a prototype GMR compound that undergoes three magnetic transitions upon cooling: a paramagnetic (PM) to ferromagnetic (FM) transition at  $T_C \approx 246 \text{ K}$ , an FM intermediate magnetic phase transition (IM) at  $T_{F-I} \approx 160 \text{ K}$ , and an intermediate to antiferromagnetic (AFM) transition at  $T_{I-A} \approx 158 \text{ K}$ . In  $\text{Mn}_3\text{M}'\text{X}$  antiperovskites, the Mn 3d orbitals contribute to the DOS at the Fermi level, while the Mn-X p-d

orbital hybridization broadens the conduction band across the Fermi level and drives the high conductivity. These Mn 3d electrons participate not only in the conduction behavior but also in the magnetic exchange interaction. Hence, the Mn–Mn direct exchange interaction of these 3d electrons will compete with the Mn–X–Mn magnetic coupling interaction. Moreover, the 3D network constructed by the corner-sharing  $Mn_6X$  octahedra contains 3D geometrical frustration in terms of its magnetic interactions.<sup>[80]</sup> The strong couplings among the various degrees of freedoms and the competing magnetic interactions make  $Mn_3M'A$  sensitive to subtle changes in the chemical composition, temperature, pressure, and external magnetic field.<sup>[81–84]</sup>  $Mn_3GaC$  exhibits plateau-like GMR curves versus temperature from 135 to 165 K, with a maximum MR of 50% at 5 T.<sup>[85]</sup> The GMR is associated with the field-induced AFM–FM/IM transition, where a strong correlation among the lattice, spin, and charge exists. A GMR with a larger temperature span could be observed if the AFM ground state can be effectively suppressed by an external magnetic field. However, a magnetic field as high as 240 kOe is required to suppress the AFM ground state.<sup>[72]</sup>

Chemical substitution provides an efficient way to improve the GMR in  $Mn_3GaC$ . Ni- and Zn-doped  $Mn_{3-x}Ni_xGaC$  are among the largest GMR materials, such as  $Ni_{50}Mn_{50-x}In_x$  and  $Mn_2Sb_{1-x}Sn_x$ .<sup>[86,87]</sup>  $Mn_{3-x}Ni_xGaC$  ( $x = 0.05$ ) exhibits an MR above 60% from 50 to 100 K and even 70% at 50 and 60 K (Figure 4a–d).<sup>[73]</sup> The MR and temperature span are significantly increased compared with the parent  $Mn_3GaC$ . For compounds with  $x = 0.1$ , the MR reaches 70% below 40 K, with a larger hysteresis than that for compounds with  $x = 0.05$ . The hysteresis indicates a first-order field-induced transition. A higher magnetic field can significantly lower the onset temperature of

the  $T_{I-A}$  phase transition, and when the magnetic field is up to 50 kOe, the  $M(T)$  curve can be remarkably enhanced at low temperature. For the  $M(H)$  curves between 50 and 120 K (below  $T_{I-A}$  in zero field), the sharp increase of  $\approx 70$  emu  $g^{-1}$  in certain fields represents an AFM to IM/FM magnetic phase transition. Above 120 K, the curves exhibit FM behavior corresponding to the small MRs (<20%). The  $M(H)$  curves at 20 K exhibit AFM behavior, where no MR is observed, while above 120 K, they exhibit ferromagnetic behavior corresponding to the small MR (<20%), which indicates that the GMR effect is closely related to the field-induced AFM–IM/FM transition. The substitution of Ni can be seen as electron-type doping that benefits the FM/IM states and weakens the rigid AFM ground state, leading to the improvement of the GMR effects.

$Mn_3Ga_{1-x}Zn_xC$  with  $x = 0.2$  exhibits the highest MR of 60% at 40 kOe, covering a broad temperature region.<sup>[88]</sup> The IM and FM states can be well distinguished under an applied field of  $\approx 1$  kOe. Under a higher field above 1 kOe, the  $M(T)$  curves gradually increase, rather than the sharp Ni-doped transition (Figure 4e). Likewise, the  $M-H$  curves show similar gradual changes (Figure 4f), indicating that the magnetic transformation induced by an external field is incomplete under moderate magnetic fields. Intrinsic minor-hysteresis-loop measurements show the incomplete transitions between the competing magnetic phases, which suggests that the field-induced AFM–FI transition is characterized by phase coexistence and metastability and is also highly relevant to the reconstruction of the electronic band structure in the magnetic fields. In the  $Mn_{3+x}Sn_{1-x}C$  system,<sup>[89]</sup> both  $Mn_3SnC$  and  $Mn_{3.1}Sn_{0.9}C$  were reported to have very small MRs of less than 4%, with a paramagnetic to ferromagnetic phase transition around  $T_c \approx 279$  K.<sup>[90]</sup> The abrupt increase in resistivity

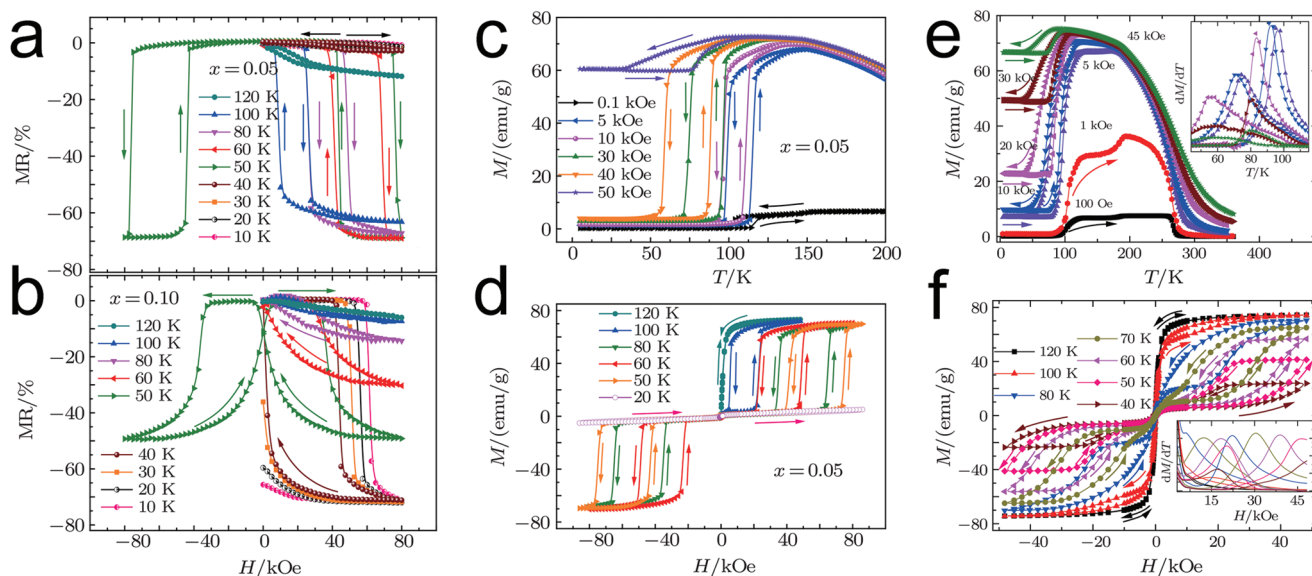


**Figure 4.** Magnetoresistance in Mn-based antiperovskite carbides. a,b)  $MR(H)$  for  $Mn_{3-x}Ni_xGaC$  with  $x = 0.05$  and  $0.1$ . c) Magnetization  $M(T)$  measured at different fields under both warming and cooling processes for  $Mn_{3-x}Ni_xGaC$  with  $x = 0.05$ . d) Field-dependent magnetization  $M(H)$  measured at selected temperatures for  $Mn_{3-x}Ni_xGaC$  with  $x = 0.05$ .<sup>[73]</sup> Adapted with permission.<sup>[73]</sup> Copyright 2009, AIP Publishing LLC. e)  $M(T)$  for  $Mn_3Ga_{0.8}Zn_{0.2}C$  under both field-cooled cooling and field-cooled warming processes in different magnetic fields. The inset shows the plots of  $dM/dT$  versus  $T$ . f)  $M(H)$  at several selected temperatures from 120 to 40 K. The inset shows the plots of  $dM/dH$  versus  $H$ .<sup>[88]</sup> Reproduced with permission.<sup>[88]</sup> Copyright 2010, AIP Publishing LLC.

versus temperature originates from the sharp decrease in the effective number of conduction electrons, resulting from the shift of the Fermi surface associated with the structural transition. Partial substitution of Sn by Zn can change the FM (or FI) state to AFM at  $\approx 170$  and  $142$  K for  $\text{Mn}_3\text{Zn}_{0.4}\text{Sn}_{0.6}\text{C}$  and  $\text{Mn}_3\text{Zn}_{0.5}\text{Sn}_{0.5}\text{C}$ , respectively. More importantly, it can improve the MR of  $\text{Mn}_3\text{Zn}_{0.5}\text{Sn}_{0.5}\text{C}$  to 34% at 95 K under a field of 12 T.

Mn-based antiperovskites show a considerable MCE comparable to those observed in the typical giant MCE materials. In Mn self-doped  $\text{Mn}_{3+x}\text{Ga}_{1-x}\text{C}$ ,<sup>[91]</sup> the  $-\Delta S_{\text{M}}(T)$  peak grows wider and exhibits a table-like curve versus temperature at  $x = 0.08$ . The largest relative cooling power (RCP) is  $\approx 301$  J kg<sup>-1</sup> at  $\approx 296.5$  K with  $\Delta H = 45$  kOe when  $x = 0.07$ , which is nearly 40% larger than that of the parent  $\text{Mn}_3\text{GaC}$  for the same magnetic field change. In  $\text{Mn}_3\text{Ga}_{1-x}\text{Al}_x\text{C}$ ,<sup>[92]</sup> the magnetic entropy change  $-\Delta S_{\text{M}}^{\text{max}}$  decreases from  $4.19$  J kg<sup>-1</sup> K for  $x = 0$  to  $2.11$  J kg<sup>-1</sup> K for  $x = 0.15$  under  $\Delta H = 45$  kOe, while the RCP gradually increases due to the broadening of the  $-\Delta S_{\text{M}}(T)$  peak and reaches a maximum of  $293$  J kg<sup>-1</sup> at  $\approx 312$  K for  $x = 0.15$ . In  $\text{Mn}_{2.9}\text{Ni}_{0.1}\text{GaC}$ , the RCP is enhanced to  $285.5$  J kg<sup>-1</sup> with  $\Delta H = 45$  kOe at  $\approx 260$  K.<sup>[93]</sup> When Ga is completely substituted by Al,<sup>[94,95]</sup> the maximum magnetic entropy change  $-\Delta S_{\text{M}}^{\text{max}}$  reaches  $3.28$  J kg<sup>-1</sup> K at  $\Delta H = 45$  kOe, and the RCP is  $328$  J kg<sup>-1</sup>, which is 1.5 times that of  $\text{Mn}_3\text{GaC}$ . The RCP is 80% that of Gd, which is the only material used in most magnetic refrigeration prototypes. In addition to the relatively large RCP and adjustable broad working temperature, the antiperovskite  $\text{Mn}_3\text{M}'\text{A}$  compounds have advantages as a refrigerant material, such as their abundant, low-cost, and non-noxious raw materials, good stability, easy fabrication and shaping, good conductivity, and good mechanical properties. Therefore, the antiperovskite  $\text{Mn}_3\text{M}'\text{A}$  compounds provide a promising alternative material system for pursuing new large MCE materials at room temperature.

### 4.3. Emergence of Superconductivity in Antiperovskites

The first observation of superconductivity in an antiperovskite was that in  $\text{Ni}_3\text{MgC}$  discovered in 2001.<sup>[96]</sup> The cubic  $\text{Ni}_3\text{MgC}$  represents an s-wave BCS-type type-II superconductor, which gives a rare example similar to the noncuprate superconductor  $\text{Ba}_{1-x}\text{K}_x\text{BiO}_3$  for exploring the superconducting mechanism. Consequently, extensive experimental and theoretical investigations were carried out on  $\text{Ni}_3\text{MgC}$ -related superconductors, such as  $\text{Ni}_3\text{CuN}$ ,  $\text{Ni}_3\text{ZnN}$ ,  $\text{Cr}_3\text{GaN}$ , and  $\text{K}_2\text{NiF}_4$ -type layered  $\text{A}_2\text{CNi}_4$  ( $\text{A} = \text{Al}, \text{Ga}, \text{Sn}$ ).<sup>[97–107]</sup> The high Ni content in the crystal structure indicates that the magnetic interactions may play a crucial role in the emergence of superconductivity. Ni K-edge X-ray absorption and <sup>13</sup>C NMR measurements and theoretical computational simulations were performed to reveal the contributions of the local structure, electronic states, and electron–phonon interactions to the superconductivity. Experimentally,  $T_{\text{c}}$  could be slightly improved by increasing the  $x$  value in  $\text{Ni}_3\text{MgC}_x$  but decreased when the Ni site was doped with other transition metals, such as Mn, Fe, Co, and Cu.

The family of ternary platinum phosphides  $\text{Pt}_3\text{AP}$  ( $\text{A} = \text{Ca}, \text{Sr}, \text{La}$ )<sup>[108]</sup> provides another interesting example of an

antiperovskite-based structure closely related to the heavy fermion superconductor  $\text{Pt}_3\text{CeSi}$ .<sup>[109]</sup> All three compounds show superconductivity at low temperatures, with the highest critical temperature of  $T_{\text{c}} = 8.4$  K for  $\text{Pt}_3\text{SrP}$ , as evidenced by the resistivity, the diamagnetic transitions, and the specific heat jump at  $T_{\text{c}}$  (Figure 5a–c). The experimental results on  $\text{Pt}_3\text{SrP}$  highlight that the charge carriers accommodated in the multiple Fermi surface pockets strongly couple with the low-lying phonons, and therefore, strong coupling superconductivity is realized at a relatively high temperature of 8.4 K. The presence of multiple Fermi surface pockets may also enhance the electron–phonon coupling by increasing the likelihood of Fermi surface nesting and the resultant phonon softening, which is consistent with the contrasting superconducting properties of  $\text{Pt}_3\text{LaP}$  and  $\text{Pt}_3\text{SrP}$ , with different Fermi surface topologies. The observation of superconductivity in centrosymmetric  $\text{Pt}_3\text{SrP}$  not only provides a unique opportunity to study the influence of no inversion symmetry on the superconductivity within similar materials but also suggests that the low-lying phonons strongly coupled with the multiple Fermi surface pockets might be the key to realizing strong coupling superconductivity at relatively high temperatures.

Superconductivity was also discovered in the so-called antiperovskites  $\text{V}_3\text{PnN}_x$  ( $\text{Pn} = \text{P}, \text{As}$ ).<sup>[110]</sup> These compounds crystallize in the filled  $\text{Re}_3\text{B}$  structure, and the positions occupied by the cations and anions are the reverse of those in the postperovskite structure. The anti-postperovskites  $\text{V}_3\text{PnN}_x$  are composed of alternately stacked  $\text{NV}_6$  octahedral layers and Pn layers, creating a quasi-2D electronic state. Bulk superconductivity is found in  $\text{V}_3\text{PN}$  and  $\text{V}_3\text{AsN}$  at  $T_{\text{c}} = 4.2$  and  $2.6$  K, respectively. Figure 5d shows the field-dependent resistivity and magnetization of  $\text{V}_3\text{PnN}_x$ , which gives the upper critical field  $H_{\text{C}2}$  of 34.9 and 27.9 kOe for  $\text{V}_3\text{PN}$  and  $\text{V}_3\text{AsN}$ , respectively, and the lower critical field  $H_{\text{C}1}$  of 207 and 134 Oe for  $\text{V}_3\text{PN}$  and  $\text{V}_3\text{AsN}$ , respectively (Figure 5e). The magnetization isotherms at 1.8 K exhibit typical type-II superconducting behavior. The superconductivity observed in N-deficient  $\text{V}_3\text{PnN}_x$  indicates that the 3d electrons of V are predominantly responsible for the emergence of superconductivity. The highest  $T_{\text{c}}$  reaches 5.6 K, as observed in  $\text{V}_3\text{PN}_{0.9}$ .

$\text{Sr}_{3-x}\text{SnO}$  is the first superconducting antiperovskite oxide ( $T_{\text{c}} = 5$  K).<sup>[111]</sup> Stoichiometric  $\text{Sr}_3\text{SnO}$  possesses Dirac points in its electronic structure, and possible topological odd-parity superconductivity analogous to the superfluid <sup>3</sup>He-B can be proposed in moderately hole-doped  $\text{Sr}_{3-x}\text{SnO}$  from theoretical analysis. Upon hole doping, the Fermi surfaces originating from the Dirac points merge into one Fermi surface around the  $\Gamma$  point. Figure 5f shows the unusual orbital texture of the Fermi surface in  $\text{Sr}_{3-x}\text{SnO}$  with a deformed-octahedral shape. Furthermore,  $\text{Sr}_{3-x}\text{SnO}$  could show topological superconductivity. The parity of Cooper pairs formed in  $\text{Sr}_{3-x}\text{SnO}$  reflects the orbital texture of the underlying Fermi surface, and the electrons on the Fermi surface favor the formation of odd-parity and spin-triplet pairs. Thus, Cooper pairs can have either a purely p or a d–p mixed orbital character depending on their location on the outer and inner Fermi surfaces (Figure 5g). Mirroring the rich variety of functionalities in perovskite oxides, the observation of superconductivity in  $\text{Sr}_{3-x}\text{SnO}$  uncovers unexpected properties in materials with an antiperovskite structure.

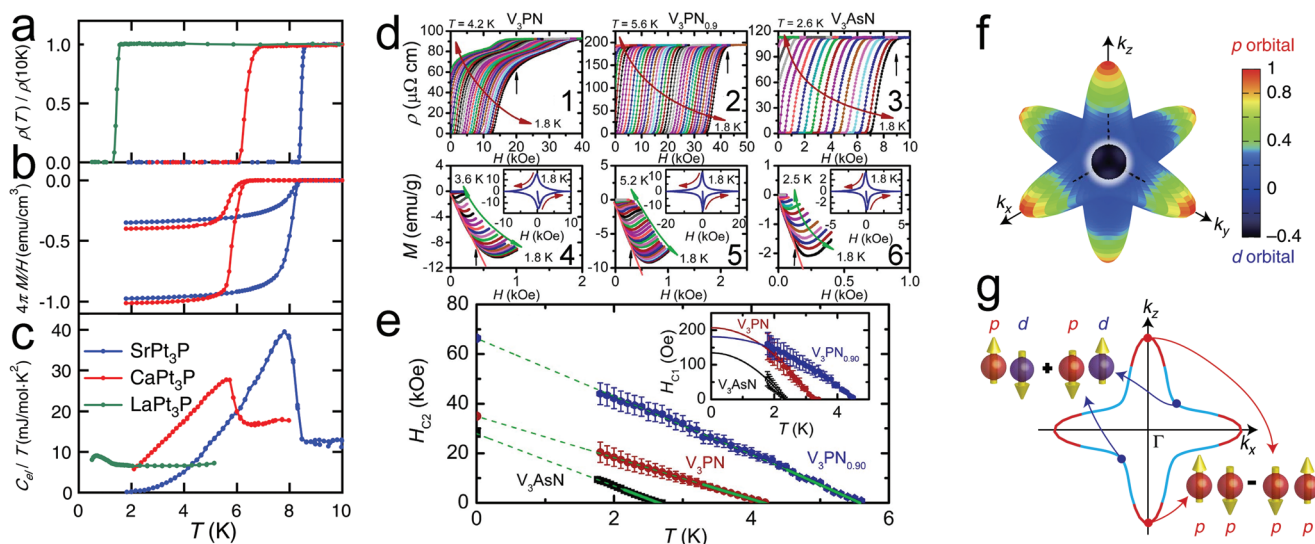


**Figure 5.** Emergence of superconductivity in antiperovskites. a–c) Superconducting transitions of  $\text{Pt}_3\text{SrP}$  in terms of the normalized resistivities, Meissner effects, and heat capacities.<sup>[108]</sup> Adapted with permission.<sup>[108]</sup> Copyright 2012, American Physical Society. d) Temperature-dependent resistivity at zero magnetic field and DC susceptibility ( $M/H$ ) curve under the ZFC condition at  $H = 1$  kOe for  $\text{V}_3\text{PnN}$  ( $\text{Pn} = \text{P}, \text{As}$ ). Arrows indicate the superconducting transition temperature ( $T_c$ ). The inset shows the low-temperature  $M/H-T$  curve under ZFC and FC conditions at  $H = 10$  Oe. e) Temperature dependence of the specific heat ( $C/T$ ) at zero magnetic field. Solid lines indicate the results of fitting with  $C = \gamma T + \beta T^3$  in the normal state and with the function based on the BCS model in the superconducting state. The inset shows the  $C_{el}/\gamma T_c$  value, where  $C_{el}$  is the electron contribution to the specific heat. The solid curve is calculated from the BCS model with an isotropic gap.<sup>[110]</sup> Adapted with permission.<sup>[110]</sup> Copyright 2013, Nature Publishing Group. f) Orbital texture of the Fermi surface of  $\text{Sr}_{3-x}\text{SnO}$  around the  $\Gamma$  point, reflecting the band inversion. The color represents the degree of mixing between the Sn-5p and Sr-4d orbital wavefunctions at each  $k$  point on the Fermi surface. g) Possible Cooper pair symmetries of  $\text{Sr}_{3-x}\text{SnO}$ .<sup>[111]</sup> Reproduced with permission.<sup>[111]</sup> Copyright 2016, Nature Publishing Group.

All the abovementioned discoveries will stimulate further exploration of new superconductors with extended antiperovskite structures. Enhancing  $T_c$  and further revealing the intrinsic relationship between the electronic and crystal structures will be goals for both material scientists and physicists. In addition, investigating the superconducting behavior of low-dimensional antiperovskites is expected to be an interesting topic in the future.

#### 4.4. Adjustable Thermal Expansion Behavior in Antiperovskites

Negative thermal expansion (NTE) is an intriguing and unconventional thermal expansion behavior resulting from the complex interplay among the lattice, electrons, and phonons of solids.<sup>[112,113]</sup> Studies on NTE materials have been a hot topic in solid-state chemistry since the discovery of isotropic NTE in  $\text{ZrW}_2\text{O}_8$  by Sleight and co-workers in 1996.<sup>[114]</sup> After that, many oxides and fluorides adopting the  $\text{ReO}_3$ -type structure with NTE behavior were developed and have been applied to compensate for the positive thermal expansion of other materials either in expansion-controlled composites or as separate components. In addition to  $\text{ZrW}_2\text{O}_8$ , a number of material systems with open-framework structures exhibit NTE behavior, such as the sodium zirconate phosphate family,<sup>[114–117]</sup>  $\text{M}_1\text{x}[\text{M}_2(\text{CN})_6]$  ( $\text{M}_1 = \text{Ag}, \text{Fe}$ ;  $\text{M}_2 = \text{Fe}, \text{Co}$ ),<sup>[118–120]</sup> and  $\text{ScF}_3$ -derived fluorides.<sup>[121]</sup> In such materials, the NTE is believed to arise from low-frequency vibrations involving the correlated motion of the corner-sharing polyhedra.

Manganese antiperovskites  $\text{Mn}_3\text{BA}$  ( $\text{B} = \text{Zn}, \text{Cu}, \text{Ni}, \text{Ge}, \text{Sn}$ ;  $\text{A} = \text{N}, \text{C}$ )<sup>[77,122–132]</sup> represent a unique metallic NTE family with good electric and thermal conductivity, isotropic NTE, and good mechanical performance compared to ceramic NTE materials. Unlike common ceramic NTE materials, such as  $\text{ZrW}_2\text{O}_8$ , the NTE property in most transition metal antiperovskites originates from their specific magnetic interaction evolution upon cooling, accompanied by a first-order transition with a dramatic magnetovolume effect (MVE). In other words, the NTE behavior of most magnetic antiperovskites is effectively broadening of the MVE into a wider temperature range. Frequently, an elemental alloying strategy is used to tune the NTE behavior of manganese antiperovskites, and controllable positive thermal expansion (PTE), NTE, giant NTE, and near-zero thermal expansion (ZTE) have been achieved in these materials over a wide range of temperatures. In addition, NTE is also found in the nonmagnetic antiperovskites  $\text{Na}_3\text{OBr}$  and  $\text{Na}_4\text{OI}_2$ .<sup>[133]</sup>

Antiperovskite manganese nitrides  $\text{Mn}_3\text{NA}$  ( $\text{A} = \text{Zn}, \text{Ga}$ , etc.) are well known for their large MVE and have been proposed as potential candidates for observing large NTE effects. As shown in **Figure 6a,b**, the lattice volumes for  $\text{A} = \text{Ga}$  and  $\text{Zn}$  compounds exhibit a sharp and pronounced increase with decreasing temperature at 290 and 165 K, respectively. Most importantly, these lattice anomalies are associated with dramatic magnetic structure transitions (i.e., an antiferromagnetic transition to the triangular  $\Gamma^{5g}$  spin structure, as revealed by neutron diffraction studies<sup>[90]</sup>). Partial elemental doping (such as Ge) at the A sites and increasing the dopant concentration can effectively broaden the MVE transition to produce NTE

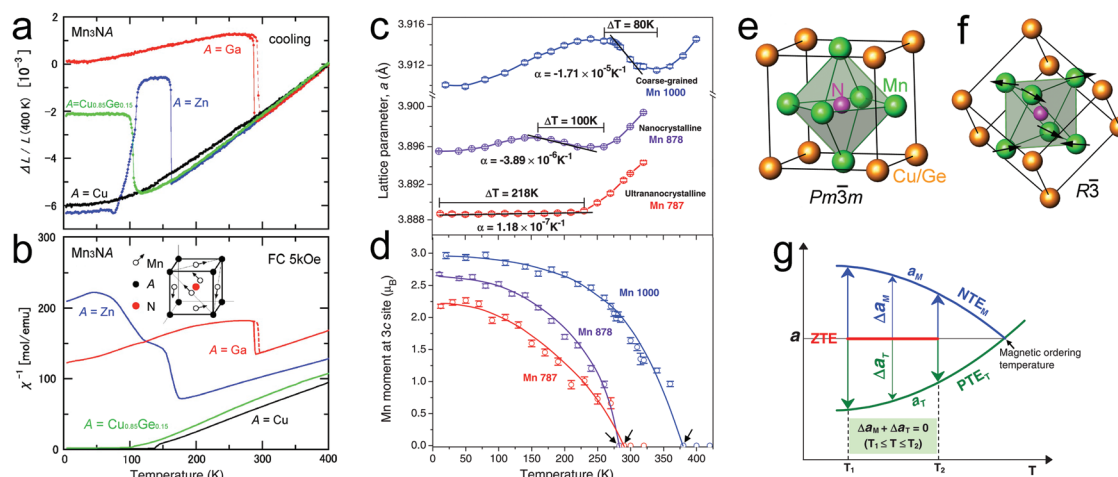


**Figure 6.** Adjustable NTE and ZTE in antiperovskite manganese nitrides. a) Linear thermal expansion and b) inverse magnetic susceptibility of  $\text{Mn}_3\text{NA}$ .<sup>[123]</sup> Solid line: cooling process; dashed line: warming process.  $\Delta L/L$  is directly related to the volume ( $V$ ) expansion in the manner of  $\Delta L/L = (1/3)\Delta V/V$ . The inset shows the antiferromagnetic  $\Gamma^{5g}$  spin structure of  $\text{Mn}_3\text{ZnN}$  and  $\text{Mn}_3\text{GaN}$ . Adapted with permission.<sup>[123]</sup> Copyright 2005, AIP Publishing LLC. c) Thermal expansion behavior of three  $\text{Mn}_3\text{Cu}_{0.5}\text{Ge}_{0.5}\text{N}$  materials with different microstructural length scales. d) Magnetic moments of the three materials as a function of temperature. The arrows indicate the magnetic ordering transition temperatures. The error bars in the figures indicate the standard deviation. e) Cubic antiperovskite crystal structure obtained from the refinement of neutron powder diffraction intensity data. f) Magnetic structure proposed from the refinement of neutron powder diffraction intensity data. The arrows indicate the magnetic moment directions. g) Mechanism for the occurrence of ZTE.  $\text{NTE}_M$  and  $\text{PTE}_T$  denote the NTE caused by magnetic ordering and the PTE caused by temperature, respectively, and  $a_M$  and  $a_T$  are the corresponding lattice parameters.  $\Delta a_M$  and  $\Delta a_T$  are the changes in the lattice parameters caused by magnetic ordering and temperature, respectively. In the temperature range between  $T_1$  and  $T_2$ , where  $\Delta a_M + \Delta a_T = 0$ , the ZTE behavior occurs.<sup>[134]</sup> Reproduced with permission.<sup>[134]</sup> Copyright 2011, Wiley-VCH.

over a wider temperature range. For example,  $\text{Mn}_3(\text{Cu}_{0.53}\text{Ge}_{0.47})\text{N}$  and  $\text{Mn}_3(\text{Cu}_{0.5}\text{Ge}_{0.5})\text{N}$  show an NTE of  $\alpha = -16 \times 10^{-6} \text{ K}^{-1}$  at  $T = 267\text{--}342$  ( $\Delta T = 75 \text{ K}$ ) and  $\alpha = -12 \times 10^{-6} \text{ K}^{-1}$  at  $T = 280\text{--}365$  ( $\Delta T = 85 \text{ K}$ ), respectively.<sup>[123]</sup>

The thermal expansion behavior in Mn-based antiperovskite nitrides can be rationally controlled by modulating the occupancy of the transition metal ions at their lattice sites.  $\text{Mn}_3\text{Cu}_{0.5}\text{Ge}_{0.5}\text{N}$ <sup>[134]</sup> demonstrates that the degree and rate of the magnetic ordering with temperature and, hence, the amount and rate of NTE with temperature can be dominated by the Mn site occupancy. Figure 6c,d shows the variations in the cubic lattice parameter  $a$  and magnetic moments at  $3c$  sites as functions of temperature. The three materials with Mn site occupancies of 100% (Mn 1000), 87.8% (Mn 878), and 78.7% (Mn 787) exhibit distinctly different characteristics of the thermal expansion behavior. For the ultranano-crystalline Mn 787, the lattice parameter  $a$  is essentially constant within the temperature range of 12–230 K, with a minuscule CTE of  $\alpha = 1.18 \times 10^{-7} \text{ K}^{-1}$ . The drastically extended ZTE temperature range, with  $\Delta T = 218 \text{ K}$ , is 3–4 times larger than those of previously reported manganese nitride antiperovskites. Figure 6e,f shows the cubic antiperovskite crystal structure ( $Pm\bar{3}m$ ) and rhombohedral magnetic structure ( $R\bar{3}$ ) of  $\text{Mn}_3\text{Cu}_{0.5}\text{Ge}_{0.5}\text{N}$ . The Cu/Ge, N and Mn atoms are located at the  $1a$  (0, 0, 0),  $1b$  (1/2, 1/2, 1/2), and  $3c$  (0, 1/2, 1/2) sites, respectively. Figure 6g shows the proposed mechanism of the ZTE occurring in the ultranano-crystalline Mn 787. Below the magnetic ordering temperature, NTE is induced, leading to an expanded lattice parameter  $a_M$ . When the contribution to the lattice expansion from magnetic ordering ( $\Delta a_M$ ) is larger than the temperature-induced thermal contraction ( $\Delta a_T$ ), the NTE behavior appears. Due to

the reduced degree of magnetic ordering caused by the low Mn site occupancy, the lattice expansion compensates for the thermal contraction, and thus, ZTE ( $\Delta a_M + \Delta a_T = 0$ ) is observed over a wide temperature range ( $\Delta T = T_2 - T_1$ ). The dependence of the NTE or ZTE performance on the Mn site occupancy suggests the possibility of tailoring the thermal expansion behavior and operating temperature range of Mn-based antiperovskites and other magnetoelastic materials.

In summary, NTE materials have been well developed in the last two decades, and antiperovskites have been well demonstrated as specific members of the NTE family. The NTE in antiperovskite materials can be expected to be modulated via further structural design efforts, theoretical predictions and especially magnetostructural coupling. Future work may also focus on multifunctionalization of NTE antiperovskites, multiple ways to control their thermal expansion, NTE enhancement, and so on.

#### 4.5. Antiperovskites as Host Lattices for Luminescent Materials

Alkaline-earth metal silicates  $\text{AE}_2\text{SiO}_5$  (AE = Ca, Sr, Ba)<sup>[135–137]</sup> and alkaline-earth metal fluoroaluminates  $\text{AE}_3\text{AlO}_4\text{F}$  (AE = Ca, Sr, Ba) have recently aroused intense research interest as the host lattices of new luminescent materials due to their good chemical stability and tunable luminescence performance. Both families can be derived from the antiperovskite-type structure in a hierarchical sense with  $\text{MO}_4$  ( $M = \text{Si}, \text{Al}$ ) tetrahedral building blocks located at the A sites of the antiperovskite structure. Park et al. first reported the  $\text{Eu}^{2+}$ -doped  $\text{Sr}_3\text{SiO}_5$  as an efficient orange-yellow emitter (centered at  $\approx 580 \text{ nm}$ ).<sup>[138]</sup>

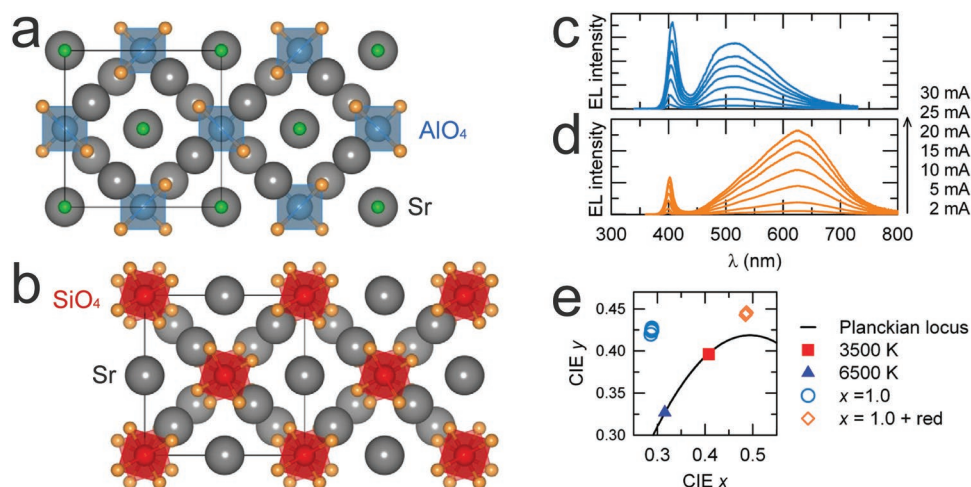


**Figure 7.** Crystal structures and luminescence of antiperovskites  $AE_3MO_4F$  ( $AE = Sr, Ba; M = Si, Al$ ). a,b) Crystal structures of  $Sr_3AlO_4F$  and  $Sr_3SiO_5$  showing similar antiperovskite-type frameworks. The light gray, blue, brown, orange, and green spheres represent the Sr, Al, Si, O, and F atoms, respectively.<sup>[140]</sup> Adapted with permission.<sup>[140]</sup> Copyright 2013, Elsevier. c,d) Luminescence of the InGaN LED ( $\lambda_{max} = 405$  nm) integrated with  $Sr_{3-x}Ba_xAlO_4F:Ce^{3+}$  ( $x = 1.0$ ) and  $Sr_{3-x}Ba_xAlO_4F:Ce^{3+}$  ( $x = 1.0$ ) + commercial red phosphors under different forward bias currents. e) CIE chromaticity coordinates of the device under different forward bias currents (as in panels (c) and (d)). The Planckian locus line and the points corresponding to color temperatures of 3500 and 6500 K are indicated.<sup>[154]</sup> Reproduced with permission.<sup>[154]</sup> Copyright 2010, American Chemical Society.

Subsequent research efforts, including  $Ba^{2+}$  ion doping in  $Eu^{2+}$ -doped  $Sr_3SiO_5$ , successfully shifted the yellow emission to longer wavelengths near 600 nm.<sup>[139]</sup> Compared to the commercial yellow phosphor  $YAG:Ce^{3+}$  for white light-emitting diodes, the antiperovskite-type hosts can overcome or partially overcome the drawbacks of the packaged products, such as the low color rendering index (CRI) and high color temperature.

Benefiting from the feasibility of antiperovskite-type structures, the host lattice and luminescence performance can be tuned in a pretty wide range via elemental substitution or a solid solution method. This strategy has been frequently demonstrated within both the  $AE_3SiO_5$  and  $AE_3AlO_4F$  systems and their solid solutions, i.e.,  $AE_3SiO_5-AE_3AlO_4F$ . **Figure 7a,b** displays the crystal structures of  $Sr_3AlO_4F$  and  $Sr_3SiO_5$  along the [001] direction, which evidently shows their structural similarity, forming a continuous solid solution over the entire composition range.  $Sr_3AlO_4F$  belongs to the tetragonal  $Cs_3CoCl_5$ -type antiperovskite structure (space group  $I4/mcm$ ) and is very closely related to  $Sr_3SiO_5$  (space group  $P4/ncc$ ), which can be written as  $Sr_3SiO_4O$  with oxygen replacing the F atoms. In the unit cell of  $Sr_3AlO_4F$ , all the  $AlO_4$  tetrahedra are well aligned, while in  $Sr_3SiO_5$ , the  $SiO_4$  tetrahedra rotate relative to each other, leading to a lower symmetry. The solid solution of  $Sr_3AlO_4F$  and  $Sr_3SiO_5$  activated with  $Ce^{3+}$  exhibits asymmetric yellow-orange emission bands that can be broadened and shifted to longer wavelengths when coactivated with  $Tb^{3+}$ . When combined with blue InGaN LEDs, the  $Tb^{3+}/Ce^{3+}$  codoped  $Sr_3AlO_4F-Sr_3SiO_5$  solid solution phosphor exhibits a high CRI and excellent correlated color temperature,<sup>[140]</sup> which demonstrates the potential use of antiperovskite solid solution phosphors in white light-emitting diodes. Many other examples of antiperovskite or antiperovskite-derived structures with or without elemental substitution as advanced host lattices for luminescent materials can also be found, such as  $Sr_3MO_4F$  ( $M = Al, Ga, In$ )<sup>[141-144]</sup> and  $AE_{3-x}A_xSiO_4F$  ( $AE = Ca,$

$Sr; A = Li, Na$ ).<sup>[145-148]</sup> Moreover, the persistent luminescence of  $Eu^{2+}$ -activated  $AE_3SiO_5$  ( $AE = Sr, Ba$ ) phosphors has also been frequently investigated.<sup>[149-153]</sup>

Ce-doped  $(Sr,Ba)_3AlO_4F$  ( $SBAF:Ce^{3+}$ ) has been developed as a highly efficient green oxyfluoride phosphor family for solid-state white light-emitting diodes.<sup>[154]</sup> In the antiperovskite structure of  $(Sr,Ba)_3AlO_4F$ , Sr and Ba occupy the  $8h$  and  $4a$  sites, respectively, and the  $4b$  site is fully occupied by Al. The eight-fold coordinated Sr sites ( $SrO_6F_2$ ) and tenfold coordinated Ba sites ( $BaO_8F_2$ ) are desirable for lanthanide ion doping. The resulting  $SBAF:Ce^{3+}$  phosphor emits a green output (centered at 502 nm) under excitation at 405 nm, with a quantum efficiency approaching 100%. When  $Sr_2BaAlO_4F:Ce^{3+}$  is incorporated with an ultraviolet LED (405 nm), greenish-white light with a CRI of 62 is obtained under a forward bias current of 20 mA. **Figure 7c-e** shows the electroluminescence spectra from a device fabricated with the  $Sr_2BaAlO_4F:Ce^{3+}$  phosphor on a 405 nm InGaN LED under forward bias currents varying from 2 to 30 mA. From the observed CIE chromaticity coordinates of (0.28, 0.42) and color temperature of 6900 K at 20 mA, the bare  $Sr_2BaAlO_4F:Ce^{3+}$  phosphor pumped by a blue LED achieves a CRI value of  $\approx 62$ . The further addition of proprietary red components to the phosphor can improve the CRI to 87.

Owing to the excellent tolerance of the antiperovskite-type structure to many elements, much room for the future exploration of novel host materials remains. For instance, a series of oxonitridosilicate oxides,  $RE_3[SiON_3]O$  ( $RE = La, Ce, Pr, Gd$ ) with antiperovskite structures, were reported by Schnich's group.<sup>[155]</sup> In the crystal structure, two different RE atoms are located at the vertices of the elongated  $ORE_6$  octahedra, and the isolated  $SiON_3$  tetrahedra are located in the cavities of the corner-sharing  $ORE_6$  frameworks. Obviously, these compounds with multiple doping sites and the incorporation of weakly electronegative elements (N) are desirable for application as the host lattice for novel luminescent materials.

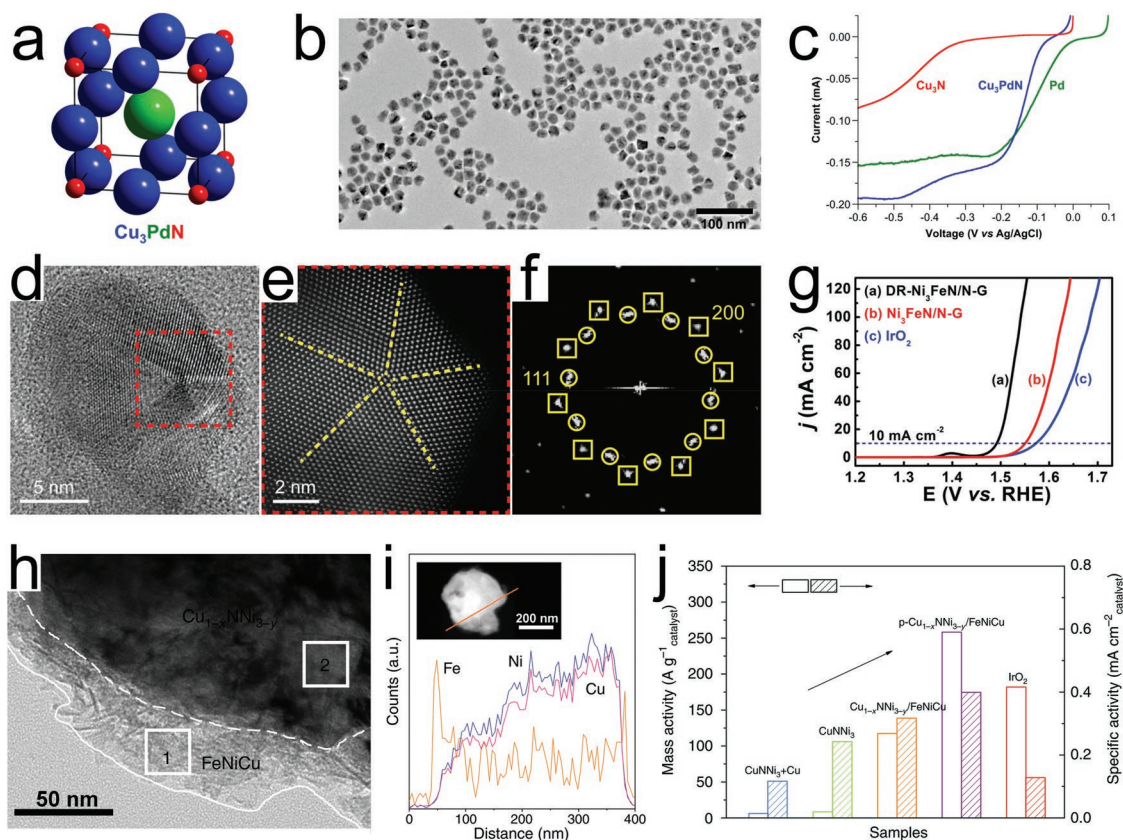


**Figure 8.** Crystal structure, morphology, and properties of antiperovskite materials. a–c) Crystal structures, morphology, and ORR performance of  $\text{Cu}_3\text{PdN}$  in 0.1 M KOH.<sup>[157]</sup> Adapted with permission.<sup>[157]</sup> Copyright 2014, American Chemical Society. d–f) Representative HRTEM and HAADF-STEM images and FFT patterns for the fivefold twinned crystal structure of defect-rich  $\text{Ni}_3\text{FeN}$ . g) OER performance of defect-rich  $\text{Ni}_3\text{FeN}$  compared with no-defect  $\text{Ni}_3\text{FeN}$  and  $\text{IrO}_2$ .<sup>[161]</sup> Adapted with permission.<sup>[161]</sup> Copyright 2018, Wiley-VCH. h,i) Magnified TEM image and line-scan EDS spectra of  $p\text{-Ni}_{3-y}\text{Cu}_{1-x}\text{N}/\text{FeNiCu}$ . j) Mass activity and BET surface area-normalized intrinsic activities of  $\text{Ni}_{3-y}\text{Cu}_{1-x}\text{N}/\text{FeNiCu}$  (oxy)hydroxide.<sup>[35]</sup> Reproduced with permission.<sup>[35]</sup> Copyright 2018, Nature Publishing Group.

#### 4.6. Antiperovskites for Electrochemical Energy Conversion and Storage

In recent years, the use of hydrogen fuel cells<sup>[156]</sup> has been treated as a powerful and suitable approach for energy supply since the resources to form the energy carriers are almost omnipresent in the form of water and air. Strong electrical energy in the form of hydrogen and oxygen is realized by a series of electrocatalytic reactions, that is, the oxygen reduction reaction (ORR), the hydrogen oxidized reaction (HOR), the hydrogen evolution reaction (HER) and the OER. These reactions take place on the electrodes, and thus, searching for efficient and durable catalysts as electrodes to optimize the catalytic process (maximum conversion efficiencies and stability and minimum energy losses) has always been a challenge.

A great variety of electrocatalysts, including precious metals, transition metals, and metal-free materials, have been extensively studied on the basis of numerous nanosynthesis strategies. Since antiperovskites can accommodate different metal elements at their X and A crystallographic sites, they are inherently designable as multifunctional catalysts when electrocatalytically active species (transition metals or precious metals) are introduced into their lattice. The first example of

an antiperovskite investigated as an efficient ORR catalyst is  $\text{Cu}_3\text{PdN}$  nanocrystals with a uniform size of  $\approx 20$  nm obtained by the solution-phase (oleylamine and 1-octadecene) synthesis method (Figure 8a–c).<sup>[157]</sup> The pure compound exhibits an ORR performance with a half-wave potential of  $-0.13$  V (vs Ag/AgCl) in 0.1 M KOH solution, which is only 60 mV more negative than that of noble metal Pd ( $-0.07$  V vs Ag/AgCl). Moreover,  $\text{Cu}_3\text{PdN}$  exhibits higher mass activities and stability compared with commercial Pd. Shortly afterward, a noble-metal-free antiperovskite embedded in nitrogen-doped carbon,  $\text{Co}_3\text{InC}_{0.75}\text{@CN}_x$ , was developed as an efficient ORR catalyst.<sup>[158]</sup> Its ORR onset potential (in 0.1 M KOH) was reported to be 0.84 V, yet its true chemical composition and the indium catalytic role remain debated. Similarly, nanohybrid  $\text{Co}_3\text{ZnN@N-CB}$  (carbon black) obtained via direct nitridation of metallic salts can serve as an efficient non-noble bimetallic ORR electrocatalyst.<sup>[159]</sup> The onset potentials for the nitride catalysts are  $\approx 0.9$  V, and the half-wave potentials are  $\approx 0.829$  V, 30 mV less than that of commercial 20 wt% Pt/C. Generally, these studies on the catalytic performance of bimetallic antiperovskites are inspiring. However, their ORR performances in acid media were not investigated, and their active sites were not discussed. In addition, rotating ring disk electrode measurements for these catalysts

are still required to reveal their true electron transfer numbers during the ORR process.

The nickel-based antiperovskite  $\text{Ni}_3\text{FeN}$  exhibits efficient overall water splitting electrocatalytic activity.<sup>[160]</sup> When using NiFe-LDH nanosheets as precursors for thermal ammonolysis,  $\text{Ni}_3\text{FeN}$  nanoparticles (size of  $\approx 100$  nm, thickness of  $\approx 9$  nm) exhibit extraordinarily high activities for both the HER and OER, with overpotentials of 158 and 280 mV at  $10 \text{ mA cm}^{-2}$  and Tafel slopes of 42 and  $46 \text{ mV dec}^{-1}$ , respectively. DFT calculations reveal that the band structure and DOS near the Fermi level are continuous, which can benefit the charge-carrier transport and electrical conductivity during catalysis. The intense energy states at Fe centers could serve as electron active sites and result in enhanced  $\text{H}_2\text{O}$  adsorption. This work demonstrates that the antiperovskite  $\text{Ni}_3\text{FeN}$  is a very promising, nonprecious metal electrocatalyst for both the OER and ORR. Encouraged by this, researchers utilized a nanomaterial synthesis strategy to optimize its catalytic properties. When loaded on graphene,<sup>[161]</sup>  $\text{Ni}_3\text{FeN}$  exhibits rich defects, such as twin crystal defects or grain boundaries (also including five-fold twinned crystals and microtwinning structures, as shown in Figure 8d–f), which leads to an enhanced OER performance with an onset overpotential of 0.22 V at  $10 \text{ mA cm}^{-2}$ . In Figure 8g, we can clearly see that the overpotential of the antiperovskite  $\text{Ni}_3\text{FeN}$  composite is much smaller than those of the defect-free sample (0.27 V) and commercial  $\text{IrO}_2$  (0.28 V). At  $\eta = 350$  mV, the current density of the composite can reach  $172.3 \text{ mA cm}^{-2}$ , which is 13.7 times that of the  $\text{IrO}_2$  catalyst. Its smaller Tafel slope ( $38 \text{ mV dec}^{-1}$ ) and higher TOF value ( $0.46 \text{ s}^{-1}$  at  $\eta = 350$  mV) further confirming its superior OER catalytic activity. Meanwhile, when loaded on reduced graphene oxide (r-GO) aerogels,<sup>[162]</sup> the resultant  $\text{Ni}_3\text{FeN}/\text{r-GO}$  materials can exhibit a greatly enhanced HER performance (overpotential of 94 mV) while maintaining an efficient OER performance (overpotential of 270 mV) in alkaline media.  $\text{Ni}_3\text{FeN}/\text{r-GO}$  was used as both the cathode and the anode to build an alkaline electrolyzer, and a  $10 \text{ mA cm}^{-2}$  current density at 1.60 V with a durability of 100 h for overall water splitting was successfully achieved. DFT calculations reveal that the surface electronic structure of  $\text{Ni}_3\text{FeN}$  is tuned by transferring electrons from the  $\text{Ni}_3\text{FeN}$  clusters to the r-GO through the interaction of the two metal species.

Based on the excellent OER performance of nickel-based antiperovskites, researchers have attempted to assemble zinc-air batteries with alkaline electrolytes using hybridized nanomaterials. The hybridized  $\text{Ni}_3\text{FeN}$ -supported  $\text{Fe}_3\text{Pt}$  intermetallic nanoalloy catalyst shows both superior ORR and OER performance comparable to those of the state-of-the-art ORR catalyst (Pt/C) and OER catalyst (Ir/C).<sup>[163]</sup> The bimetallic nitride  $\text{Ni}_3\text{FeN}$  mainly contributes to the high activity for the OER, while the ordered  $\text{Fe}_3\text{Pt}$  nanoalloy contributes to the excellent activity for the ORR. The  $\text{Fe}_3\text{Pt}/\text{Ni}_3\text{FeN}$  bifunctional catalyst enables Zn-air batteries to achieve a long-term cycling performance of over 480 h at  $10 \text{ mA cm}^{-2}$  with high efficiency. As shown in another work, when precious metals are not involved, the hybrid  $\text{Ni}_3\text{FeN}/\text{Co}$ , N-carbon nanoframe shows an overall potential gap  $\Delta E$  of 0.69 V, better than that of the Pt/C- $\text{IrO}_2$  mixture (0.77 V).<sup>[164]</sup> Impressively, the battery displayed very stable operation over a 540 h test with an initial  $\Delta E$  of 0.79 V

at a current density of  $6 \text{ mA cm}^{-2}$  and could withstand a high current density of  $50 \text{ mA cm}^{-2}$  while maintaining a low voltage gap of 1.15 V during a 136 h test. More recently, an antiperovskite-based porous  $\text{Ni}_{3-y}\text{Cu}_{1-x}\text{N}/\text{FeNiCu}$  (p- $\text{Ni}_{3-y}\text{Cu}_{1-x}\text{N}/\text{FeNiCu}$ ) (oxy)hydroxide core-shell structured hybrid was reported as a high performance OER catalyst with excellent activity and durability.<sup>[35]</sup> As shown in Figure 8h, close observation reveals a distinct  $\text{Ni}_{3-y}\text{Cu}_{1-x}\text{N}-\text{FeNiCu}$  interface (as indicated by the white dashed line). In the core-shell structure, Fe is located across the entire area and possesses strong signals in the shell region (Figure 8i). The as-obtained product needs an overpotential of only 280 mV to drive  $10 \text{ mA cm}^{-2}$ , and when the product is fixed at this current density for the stability test, its potential remains almost unchanged throughout the entire 24 h test. Figure 8j plots the mass activity and specific activity of the various electrocatalysts at  $\eta = 400$  mV (1.63 V vs RHE). The mass activity of p- $\text{Ni}_{3-y}\text{Cu}_{1-x}\text{N}/\text{FeNiCu}$  is  $258.3 \text{ Ag}^{-1}$ , 1.5 times that of  $\text{IrO}_2$  electrocatalysts. The intrinsic OER activity of the various catalysts follows the order of  $(\text{Ni}_3\text{CuN}+\text{Cu}) < \text{IrO}_2 < \text{Ni}_3\text{CuN} < \text{Ni}_{3-y}\text{Cu}_{1-x}\text{N}/\text{FeNiCu} < \text{p-Ni}_{3-y}\text{Cu}_{1-x}\text{N}/\text{FeNiCu}$ , which indicates the attractive activity of antiperovskites and the highest OER performance for the p- $\text{Ni}_{3-y}\text{Cu}_{1-x}\text{N}/\text{FeNiCu}$  catalyst. This excellent OER activity can be ascribed to the unique advantage of the core-shell structure, as well as to the synergistic effect of Fe, Ni and Cu and the highly porous hierarchical structure. The antiperovskite core not only acts as a conductive substrate but also plays a vital role in promoting the OER performance during electrocatalysis.

In summary, the investigation of antiperovskites for electrochemical applications may open a new field in developing novel materials for energy generation and storage. Taking advantage of numerous controllable nanosynthesis methodologies and material design principles, one may extend the application of antiperovskite-based nanomaterials to Li-batteries,<sup>[165]</sup>  $\text{CO}_2$  or  $\text{N}_2$  electroreduction,<sup>[166,167]</sup> and more catalytic systems that arouse general interest. Substituting precious-metal catalysts with low-cost antiperovskites is expected to be a new direction. Producing hybridized antiperovskite-based materials as multifunctional HER, OER or ORR catalysts will be another interesting pathway to achieve metal-air batteries and overall water splitting electrolyzers.

#### 4.7. Other Emerging Functionalities of Antiperovskites

Antiperovskites also exhibit other emerging properties such as ferromagnetic shape memory effects and giant magnetostriction in some manganese nitride antiperovskites.<sup>[168–170]</sup> A new family of 3D topological insulators with an antiperovskite structure has been proposed based on first-principles calculations.<sup>[171]</sup> A near-zero temperature coefficient of resistivity was observed in the antiperovskite  $\text{Mn}_3\text{Ni}_{1-x}\text{Cu}_x\text{N}$ .<sup>[172]</sup> The  $(\text{AE}_3\text{N})\text{Bi}$  (AE = Ca, Sr, Ba) family is chemically inert, and the lattice is well matched to important semiconductors, which provides a platform for easy integration with electronic devices. Moreover, recently developed antiperovskite-type organic-inorganic hybrids that can serve as new ferroelectrics<sup>[173,174]</sup> enrich the antiperovskite family and extend the application scope of multifunctional antiperovskites.

Antiperovskites also show intriguing properties under external fields such as pressure and temperature. Typically,  $\text{Mn}_3\text{Ga}_{0.95}\text{N}_{0.94}$  was reported to exhibit a remarkable so-called “baromagnetic effect,”<sup>[175]</sup> i.e., a magnetic phase transition caused by external hydrostatic pressure. Piezomagnetism was studied theoretically in a series of magnetically frustrated Mn-based antiperovskite nitrides and experimentally in  $\text{Mn}_3\text{NiN}$ .<sup>[176,177]</sup> Boldrin et al. studied the multisite exchange-enhanced barocaloric response in  $\text{Mn}_3\text{NiN}$  across the Néel transition temperature.<sup>[178]</sup> All these findings highlight the potential of discovering novel materials with enhanced multifunctionalities in the broad and chemically flexible antiperovskite family.

## 5. Conclusions and Perspectives

In this review, we summarized recent explorations of antiperovskite-type materials and their intriguing functionalities for potential energy-related applications. These functionalities include their electrical and magnetic properties, ionic conductivity, superconductivity, NTE, ability to act as the host lattice for photoluminescence and electrocatalysts, etc. Nevertheless, antiperovskite-type materials are still poorly studied compared to traditional perovskites. More efforts are needed to explore new compounds with an antiperovskite structure and the new phenomena within them. Perovskite structures offer many opportunities for designing materials with unique properties based on structural chemistry approaches, such as A/B site doping and defect control. Therefore, more research to improve the performance of known materials and to understand their structure–property relationships is also desirable.

### 5.1. Exploration of New Antiperovskites

An important characteristic of antiperovskites  $\text{X}_3\text{BA}$  is their susceptibility to partial substitution at all the A, B, and X positions with a wide range of ions and valences. The flexibility of the antiperovskite-type structure enables antiperovskite materials themselves to be tuned by chemical tailoring. In light of the numerous artificial perovskites with significant applications, future research efforts are anticipated to greatly expand the structures and functionalities of antiperovskites. For example, based on a given  $\text{X}_3\text{BA}$ , we can design double antiperovskites with the formula  $\text{X}_6\text{B}_2\text{AA}'$  or  $\text{X}_6\text{BB}'\text{A}_2$ . Studying whether the A/A' and B/B' at the A and B sites are ordered or disordered and, thus, the impact of anion ordering on the physical properties will be interesting. Based on a given  $\text{X}_3\text{BA}$ , we can also design new deficient antiperovskites with a formula such as  $\text{X}_5\text{B}_2\text{A}_2$ . The valence of the transition metal ions, magnetism and potential battery performance of such deficient antiperovskites may greatly depend on the ordering of the X vacancies.

### 5.2. Antiperovskites with Novel Intergrowth Structures

Two familiar types of layered perovskites can be derived from the 3D  $\text{ABO}_3$  perovskites: the Dion–Jacobson (DJ) type with the

general formula  $\text{A}'[\text{A}_{n-1}\text{B}_n\text{O}_{3n+1}]$  and the Ruddlesden–Popper (RP) type with the formula  $\text{A}'_2[\text{A}_{n-1}\text{B}_n\text{O}_{3n+1}]$ . The thickness of the perovskite slab is given by  $n$ , which determines the number of corner-sharing  $\text{BO}_6$  octahedra along the  $c$  axis.  $\text{KCa}_2\text{Nb}_3\text{O}_{10}$  and  $\text{K}_2\text{LnTi}_3\text{O}_{10}$  are two representatives of  $n = 3$  members for the DJ and RP phases, both of which are prototypes of a series of materials with novel functionalities and interesting chemical reactivity. For example, the weakly bonded alkali ions in these layered structures can undergo ion exchange reactions and subsequent exfoliation. For antiperovskites, some intergrowth structures are already known, such as  $\text{Na}_4\text{OX}_2$  ( $\text{X} = \text{Br}, \text{I}$ ) adopting the  $\text{K}_2\text{NiF}_4$ -type structure. Can we continue to explore more interesting but complex structures such as  $(\text{XA})_m(\text{X}_3\text{AB})_n$ ,  $(\text{XA})_m(\text{X}_{1.5}\text{AB})_n$ ,  $(\text{X}_3\text{AB})_m(\text{X}'_3\text{A}'\text{B}')_n$  or  $(\text{X}_3\text{AB})_m(\text{X}'_{1.5}\text{A}'\text{B}')_n$ ? In some low-dimensional antiperovskite structures, can some low-temperature topochemical manipulations, similar to those in perovskites, be performed?<sup>[179,180]</sup>

### 5.3. Structural Manipulations toward Enhanced Performance

An important characteristic of antiperovskites is their susceptibility to partial substitution at both the A and B sites. Because of the wide range of ions and valences that this simple crystal structure can accommodate, antiperovskites lend themselves to chemical tailoring. Elemental doping and vacancy control are two commonly used strategies. Specific manipulation methods could be considered for a given structure and its unique functionality.

Another possibility is to involve small molecules at the A sites of an antiperovskite structure. One recent example is the organic–inorganic hybrid  $\text{CH}_3\text{NH}_3\text{MX}_3$  ( $\text{M} = \text{Pb}, \text{Sn}$ ;  $\text{X} = \text{Cl}, \text{Br}, \text{I}$ ) with methylammonium at the A sites for solar cell applications.<sup>[3–6]</sup> Antiperovskites  $\text{Na}_3\text{OCN}$  and  $\text{Na}_3\text{NO}_3$  with  $\text{CN}^-$  or  $\text{NO}_2^-$  groups at the A sites were reported to show high sodium ion conductivity because the aspheric groups at the A sites may induce order/disorder transitions. Such first-order phase transitions can sometimes boost the ionic conductivity by several orders of magnitude and are worth considering in solid electrolyte design.

In summary, antiperovskites are currently a rarely developed family of materials. Antiperovskites benefit from not only the built-in potential of the perovskite-type structure but also their cation-rich features. Antiperovskites are relatively simple to synthesize due to the flexibility of their structure, which enables a diverse chemistry. In light of the great possibilities of antiperovskites as functional materials, further investigations are anticipated to expand the scope of the structural and functional perspectives examined in this review and contribute greatly to the development of solid-state sciences.

## Acknowledgements

This work was financially supported by the National Natural Science Foundation of China (51825201, 51732005), the National Key Research and Development Program of China (2017YFA0206701), the National Program for Support of Top-notch Young Professionals, and the Changjiang Scholar Program.

## Conflict of Interest

The authors declare no conflict of interest.

## Author Contributions

Y.W. and H.Z. contributed equally to this work. R.Z. and Y.Z. supervised the preparation of this review article. The other authors contributed to some content and figures. All authors approved the final version of the manuscript.

## Keywords

antiperovskites, crystal structure, functionalities, material design

Received: August 3, 2019

Revised: October 12, 2019

Published online: December 9, 2019

- [1] M. D. Graef, M. McHenry, *Structure of Materials: An Introduction to Crystallography, Diffraction and Symmetry*, Cambridge University Press, Cambridge **2007**.
- [2] M. A. Pena, J. L. G. Fierro, *Chem. Rev.* **2001**, *101*, 1981.
- [3] C. C. Stoumpos, M. G. Kanatzidis, *Adv. Mater.* **2016**, *28*, 5778.
- [4] P. Gao, M. Graetzel, M. K. Nazeeruddin, *Energy Environ. Sci.* **2014**, *7*, 2448.
- [5] M. A. Green, A. Ho-Baillie, H. J. Snaith, *Nat. Photonics* **2014**, *8*, 506.
- [6] B. V. Lotsch, *Angew. Chem., Int. Ed.* **2014**, *53*, 635.
- [7] L. L. Boyer, P. J. Edwardson, *Ferroelectrics* **1990**, *104*, 417.
- [8] S. V. Krivovichev, *Z. Kristallogr.* **2008**, *223*, 109.
- [9] P. Tong, B.-S. Wang, Y.-P. Sun, *Chin. Phys. B* **2013**, *22*, 067501.
- [10] P. Tong, Y. P. Sun, *Adv. Condens. Matter Phys.* **2012**, *2012*, 903239.
- [11] R. Niewa, *Z. Anorg. Allg. Chem.* **2013**, *639*, 1699.
- [12] B. V. Beznosikov, *J. Struct. Chem.* **2003**, *44*, 885.
- [13] Y. P. Sun, P. Tong, B. C. Zhao, X. B. Zhu, W. H. Song, *Solid State Commun.* **2006**, *138*, 64.
- [14] J. C. Lin, B. S. Wang, P. Tong, W. J. Lu, L. Zhang, X. B. Zhu, Z. R. Yang, W. H. Song, J. M. Dai, Y. P. Sun, *Appl. Phys. Lett.* **2011**, *98*, 092507.
- [15] D. Kasugai, A. Ozawa, T. Inagaki, K. Takenaka, *J. Appl. Phys.* **2012**, *111*, 07E314.
- [16] S. Lin, B. S. Wang, P. Tong, L. Hu, Y. N. Huang, W. J. Lu, B. C. Zhao, W. H. Song, Y. P. Sun, *J. Appl. Phys.* **2013**, *113*, 103906.
- [17] L. Chu, C. Wang, P. Bordet, C. V. Colin, S. Pairis, Y. Na, J. Yan, Q. Huang, *Scr. Mater.* **2013**, *68*, 968.
- [18] Y. Sun, Y. Guo, Y. Tsujimoto, J. Yang, B. Shen, W. Yi, Y. Matsushita, C. Wang, X. Wang, J. Li, C. I. Sathish, K. Yamaura, *Inorg. Chem.* **2013**, *52*, 800.
- [19] Y. He, O. Y. Kontsevoi, C. C. Stoumpos, G. G. Trimarchi, S. M. Islam, Z. Liu, S. S. Kostina, S. Das, J.-I. Kim, W. Lin, B. W. Wessels, M. G. Kanatzidis, *J. Am. Chem. Soc.* **2017**, *139*, 7939.
- [20] M. Valldor, T. Wright, A. Fitch, Y. Prots, *Angew. Chem., Int. Ed.* **2016**, *55*, 9380.
- [21] K. T. Lai, I. Antonyshyn, Y. Prots, M. Valldor, *J. Am. Chem. Soc.* **2017**, *139*, 9645.
- [22] A. M. Glazer, *Acta Crystallogr., Sect. B: Struct. Sci., Cryst. Eng. Mater.* **1972**, *B28*, 3384.
- [23] A. M. Glazer, *Acta Crystallogr., Sect. A: Found. Adv.* **1975**, *A31*, 756.
- [24] M. Y. Chern, F. J. Disalvo, J. B. Parise, J. A. Goldstone, *J. Solid State Chem.* **1992**, *96*, 426.
- [25] H. Boller, *Monatsh. Chem.* **1968**, *99*, 2444.
- [26] M. Barberon, R. Madar, E. Fruchart, G. Lorthioi, R. Fruchart, *Mater. Res. Bull.* **1970**, *5*, 1.
- [27] Y. Zhao, L. L. Daemen, *J. Am. Chem. Soc.* **2012**, *134*, 15042.
- [28] M. Y. Chern, D. A. Vennos, F. J. Disalvo, *J. Solid State Chem.* **1992**, *96*, 415.
- [29] A. Houben, J. Burghaus, R. Dronskowski, *Chem. Mater.* **2009**, *21*, 4332.
- [30] M. P. Brady, S. K. Wrobel, T. A. Lograsso, E. A. Payzant, D. T. Hoelzer, J. A. Horton, L. R. Walker, *Chem. Mater.* **2004**, *16*, 1984.
- [31] W. H. Cao, B. He, C. Z. Liao, L. H. Yang, L. M. Zeng, C. Dong, *J. Solid State Chem.* **2009**, *182*, 3353.
- [32] Y. Sun, C. Wang, Y. Na, L. Chu, Y. Wen, M. Nie, *Mater. Res. Bull.* **2010**, *45*, 1230.
- [33] Y. Na, C. Wang, L. Chu, L. Ding, J. Yan, Y. Xue, W. Xie, X. Chen, *Mater. Lett.* **2011**, *65*, 3447.
- [34] H.-S. Lee, D. J. Jang, H. G. Lee, S. I. Lee, S. M. Choi, C. J. Kim, *Adv. Mater.* **2007**, *19*, 1807.
- [35] Y. Zhu, G. Chen, Y. Zhong, Y. Chen, N. Ma, W. Zhou, Z. Shao, *Nat. Commun.* **2018**, *9*, 2326.
- [36] J. M. Tarascon, M. Armand, *Nature* **2001**, *414*, 359.
- [37] E. Quartarone, P. Mustarelli, *Chem. Soc. Rev.* **2011**, *40*, 2525.
- [38] J. C. Bachman, S. Muy, A. Grimaud, H.-H. Chang, N. Pour, S. F. Lux, O. Paschos, F. Maglia, S. Lupart, P. Lamp, L. Giordano, Y. Shao-Horn, *Chem. Rev.* **2016**, *116*, 140.
- [39] A. R. Rodger, J. Kuwano, A. R. West, *Solid State Ionics* **1985**, *15*, 185.
- [40] H.-J. Deiseroth, S.-T. Kong, H. Eckert, J. Vannahme, C. Reiner, T. Zaiss, M. Schlosser, *Angew. Chem., Int. Ed.* **2008**, *47*, 755.
- [41] V. Thangadurai, S. Narayanan, D. Pinzaru, *Chem. Soc. Rev.* **2014**, *43*, 4714.
- [42] A. Martinez-Juarez, C. Pecharroman, J. E. Iglesias, J. M. Rojo, *J. Phys. Chem. B* **1998**, *102*, 372.
- [43] H. Yamane, S. Kikkawa, M. Koizumi, *Solid State Ionics* **1987**, *25*, 183.
- [44] W. Schnick, J. Luecke, *Solid State Ionics* **1990**, *38*, 271.
- [45] M. Matsuo, H. Oguchi, H. Maekawa, H. Takamura, S. Orimo, *Mater. Matters* **2010**, *5*, 4.
- [46] O. Bohnke, C. Bohnke, J. L. Fourquet, *Solid State Ionics* **1996**, *91*, 21.
- [47] S. Stramare, V. Thangadurai, W. Weppner, *Chem. Mater.* **2003**, *15*, 3974.
- [48] H. D. Lutz, P. Kuske, K. Wussow, *Solid State Ionics* **1988**, *28*, 1282.
- [49] A. Manthiram, X. Yu, S. Wang, *Nat. Rev. Mater.* **2017**, *2*, 16103.
- [50] Z. Deng, B. Radhakrishnan, S. P. Ong, *Chem. Mater.* **2015**, *27*, 3749.
- [51] S. Chandra, *Superionic Solids: Principles and Applications*, North-Holland Publ., Amsterdam **1981**.
- [52] N. Kamaya, K. Homma, Y. Yamakawa, M. Hirayama, R. Kanno, M. Yonemura, T. Kamiyama, Y. Kato, S. Hama, K. Kawamoto, A. Mitsui, *Nat. Mater.* **2011**, *10*, 682.
- [53] X. Lü, G. Wu, J. W. Howard, A. Chen, Y. Zhao, L. L. Daemen, Q. Jia, *Chem. Commun.* **2014**, *50*, 11520.
- [54] X. Lü, J. W. Howard, A. Chen, J. Zhu, S. Li, G. Wu, P. Dowden, H. Xu, Y. Zhao, Q. Jia, *Adv. Sci.* **2016**, *3*, 1500359.
- [55] M. H. Braga, J. A. Ferreira, V. Stockhausen, J. E. Oliveira, A. El-Azab, *J. Mater. Chem. A* **2014**, *2*, 5470.
- [56] K. Hippler, S. Sitta, P. Vogt, H. Sabrowsky, *Acta Crystallogr., Sect. C: Struct. Chem.* **1990**, *C46*, 736.
- [57] M. Jansen, C. Feldmann, W. Muller, *Z. Anorg. Allg. Chem.* **1992**, *611*, 7.

- [58] H. Sabrowsky, K. Hippler, S. Sitta, P. Vogt, L. Walz, *Acta Crystallogr., Sect. C: Struct. Chem.* **1990**, C46, 368.
- [59] L. Fanfani, G. Giuseppetti, C. Tadini, P. F. Zanazzi, *Mineral. Mag.* **1980**, 43, 753.
- [60] Y. Wang, Q. Wang, Z. Liu, Z. Zhou, S. Li, J. Zhu, R. Zou, Y. Wang, J. Lin, Y. Zhao, *J. Power Sources* **2015**, 293, 735.
- [61] J. Zhu, Y. Wang, S. Li, J. W. Howard, J. Neuefeind, Y. Ren, H. Wang, C. Liang, W. Yang, R. Zou, C. Jin, Y. Zhao, *Inorg. Chem.* **2016**, 55, 5993.
- [62] Y. Li, W. Zhou, S. Xin, S. Li, J. Zhu, X. Lu, Z. Cui, Q. Jia, J. Zhou, Y. Zhao, J. B. Goodenough, *Angew. Chem., Int. Ed.* **2016**, 55, 9965.
- [63] H. Fang, S. Wang, J. Liu, Q. Sun, P. Jena, *J. Mater. Chem. A* **2017**, 5, 13373.
- [64] H. Fang, P. Jena, *Proc. Natl. Acad. Sci. USA* **2017**, 114, 11046.
- [65] M. Jansen, *Angew. Chem., Int. Ed.* **1991**, 30, 1547.
- [66] W. Cho, S. Myeong, N. Kim, S. Lee, Y. Kim, M. Kim, S. J. Kang, N. Park, P. Oh, J. Cho, *Adv. Mater.* **2017**, 29, 1605578.
- [67] C. Zener, *Phys. Rev.* **1951**, 82, 403.
- [68] S. A. Wolf, D. Treger, *IEEE Trans. Magn.* **2000**, 36, 2748.
- [69] E. L. Nagaev, *Phys. Rep.* **2001**, 346, 387.
- [70] B. G. Shen, J. R. Sun, F. X. Hu, H. W. Zhang, Z. H. Cheng, *Adv. Mater.* **2009**, 21, 4545.
- [71] A. M. Tishin, *J. Magn. Mater.* **2007**, 316, 351.
- [72] K. Kamishima, T. Goto, H. Nakagawa, N. Miura, M. Ohashi, N. Mori, T. Sasaki, T. Kanomata, *Phys. Rev. B* **2000**, 63, 024426.
- [73] B. S. Wang, P. Tong, Y. P. Sun, L. J. Li, W. Tang, W. J. Lu, X. B. Zhu, Z. R. Yang, W. H. Song, *Appl. Phys. Lett.* **2009**, 95, 222509.
- [74] M. H. Yu, L. H. Lewis, A. R. Moodenbaugh, *J. Appl. Phys.* **2003**, 93, 10128.
- [75] B. S. Wang, P. Tong, Y. P. Sun, X. Luo, X. B. Zhu, G. Li, X. D. Zhu, S. B. Zhang, Z. R. Yang, W. H. Song, J. M. Dai, *EPL* **2009**, 85, 47004.
- [76] S. Iikubo, K. Kodama, K. Takenaka, H. Takagi, M. Takigawa, S. Shamoto, *Phys. Rev. Lett.* **2008**, 101, 205901.
- [77] K. Takenaka, H. Takagi, *Appl. Phys. Lett.* **2009**, 94, 131904.
- [78] K. Asano, K. Koyama, K. Takenaka, *Appl. Phys. Lett.* **2008**, 92, 161909.
- [79] Y. Nakamura, K. Takenaka, A. Kishimoto, H. Takagi, *J. Am. Ceram. Soc.* **2009**, 92, 2999.
- [80] D. Tahara, Y. Motome, M. Imada, *J. Phys. Soc. Jpn.* **2007**, 76, 013708.
- [81] K. Takenaka, T. Inagaki, H. Takagi, *Appl. Phys. Lett.* **2009**, 95, 132508.
- [82] T. Kaneko, T. Kanomata, K. Shirakawa, *J. Phys. Soc. Jpn.* **1987**, 56, 4047.
- [83] K. Kamishima, M. I. Bartashevich, T. Goto, M. Kikuchi, T. Kanomata, *J. Phys. Soc. Jpn.* **1998**, 67, 1748.
- [84] J. P. Bouchaud, R. Fruchart, R. Pauthenet, M. Guillot, H. Bartholin, F. Chaisse, *J. Appl. Phys.* **1966**, 37, 971.
- [85] W. S. Kim, E. O. Chi, J. C. Kim, H. S. Choi, N. H. Hur, *Solid State Commun.* **2001**, 119, 507.
- [86] S. Y. Yu, Z. H. Liu, G. D. Liu, J. L. Chen, Z. X. Cao, G. H. Wu, B. Zhang, X. X. Zhang, *Appl. Phys. Lett.* **2006**, 89, 162503.
- [87] Y. Q. Zhang, Z. D. Zhang, *Phys. Rev. B* **2003**, 67, 132405.
- [88] B. S. Wang, C. C. Li, J. C. Lin, S. Lin, P. Tong, X. B. Zhu, B. C. Zhao, W. J. Lu, Z. R. Yang, W. H. Song, J. M. Dai, Y. P. Sun, *Appl. Phys. Lett.* **2010**, 97, 142505.
- [89] Y. B. Li, W. F. Li, W. J. Feng, Y. Q. Zhang, Z. D. Zhang, *Phys. Rev. B* **2005**, 72, 024411.
- [90] D. Fruchart, E. F. Bertaut, *J. Phys. Soc. Jpn.* **1978**, 44, 781.
- [91] B. S. Wang, P. Tong, Y. P. Sun, X. B. Zhu, X. Luo, G. Li, W. H. Song, Z. R. Yang, J. M. Dai, *J. Appl. Phys.* **2009**, 105, 083907.
- [92] B. S. Wang, C. C. Li, S. Lin, J. C. Lin, L. J. Li, P. Tong, W. J. Lu, X. B. Zhu, Z. R. Yang, W. H. Song, J. M. Dai, Y. P. Sun, *J. Magn. Mater.* **2011**, 323, 2017.
- [93] B. S. Wang, P. Tong, Y. P. Sun, W. Tang, L. J. Li, X. B. Zhu, Z. R. Yang, W. H. Song, *Phys. B* **2010**, 405, 2427.
- [94] A. Kenmotsu, H. Watanabe, T. Shinohara, *J. Phys. Soc. Jpn.* **1972**, 32, 377.
- [95] B. S. Wang, J. C. Lin, P. Tong, L. Zhang, W. J. Lu, X. B. Zhu, Z. R. Yang, W. H. Song, J. M. Dai, Y. P. Sun, *J. Appl. Phys.* **2010**, 108, 093925.
- [96] T. He, Q. Huang, A. P. Ramirez, Y. Wang, K. A. Regan, N. Rogado, M. A. Hayward, M. K. Haas, J. S. Slusky, K. Inumara, H. W. Zandbergen, N. P. Ong, R. J. Cava, *Nature* **2001**, 411, 54.
- [97] C. M. I. Okoye, *J. Phys.: Condens. Matter* **2003**, 15, 833.
- [98] S. Mollah, *J. Phys.: Condens. Matter* **2004**, 16, R1237.
- [99] B. He, C. Dong, L. Yang, X. Chen, L. Ge, L. Mu, Y. Shi, *Supercond. Sci. Technol.* **2013**, 26, 125015.
- [100] Z. Hui, X. Tang, D. Shao, H. Lei, J. Yang, W. Song, H. Luo, X. Zhu, Y. Sun, *Chem. Commun.* **2014**, 50, 12734.
- [101] H. M. Tütüncü, G. P. Srivastava, *Philos. Mag.* **2013**, 93, 4469.
- [102] S. Ram, V. Kanchana, *Solid State Commun.* **2014**, 181, 54.
- [103] H. M. Tütüncü, G. P. Srivastava, *J. Appl. Phys.* **2013**, 114, 053905.
- [104] M. Uehara, A. Uehara, K. Kozawa, T. Yamazaki, Y. Kimishima, *Phys. C* **2010**, 470, S688.
- [105] K. Ohishi, T. U. Ito, W. Higemoto, T. Yamazaki, A. Uehara, K. Kozawa, Y. Kimishima, M. Uehara, *Phys. C* **2010**, 470, S705.
- [106] M. Uehara, A. Uehara, K. Kozawa, Y. Kimishima, *J. Phys. Soc. Jpn.* **2009**, 78, 033702.
- [107] D. F. Shao, W. J. Lu, S. Lin, P. Tong, H. B. Jian, X. Y. Pan, Y. P. Sun, *AIP Adv.* **2012**, 2, 042167.
- [108] T. Takayama, K. Kuwano, D. Hirai, Y. Katsura, A. Yamamoto, H. Takagi, *Phys. Rev. Lett.* **2012**, 108, 237001.
- [109] E. Bauer, G. Hilscher, H. Michor, C. Paul, E. W. Scheidt, A. Gribanov, Y. Seropegin, H. Noel, M. Sigrist, P. Rogl, *Phys. Rev. Lett.* **2004**, 92, 027003.
- [110] B. Wang, K. Ohgushi, *Sci. Rep.* **2013**, 3, 3381.
- [111] M. Oudah, A. Ikeda, J. N. Hausmann, S. Yonezawa, T. Fukumoto, S. Kobayashi, M. Sato, Y. Maeno, *Nat. Commun.* **2016**, 7, 13617.
- [112] J. S. O. Evans, *J. Chem. Soc., Dalton Trans.* **1999**, 19, 3317.
- [113] J. Chen, L. Hu, J. Deng, X. Xing, *Chem. Soc. Rev.* **2015**, 44, 3522.
- [114] T. A. Mary, J. S. O. Evans, T. Vogt, A. W. Sleight, *Science* **1996**, 272, 90.
- [115] R. Roy, D. K. Agrawal, H. A. McKinstry, *Annu. Rev. Mater. Sci.* **1989**, 19, 59.
- [116] J. P. Boilot, J. P. Salanie, G. Desplanches, D. Lepotier, *Mater. Res. Bull.* **1979**, 14, 1469.
- [117] G. E. Lenain, H. A. McKinstry, J. Alamo, D. K. Agrawal, *J. Mater. Sci.* **1987**, 22, 17.
- [118] A. L. Goodwin, M. Calleja, M. J. Conterio, M. T. Dove, J. S. O. Evans, D. A. Keen, L. Peters, M. G. Tucker, *Science* **2008**, 319, 794.
- [119] S. Margadonna, K. Prassides, A. N. Fitch, *J. Am. Chem. Soc.* **2004**, 126, 15390.
- [120] S. Adak, L. L. Daemen, M. Hartl, D. Williams, J. Summerhill, H. Nakotte, *J. Solid State Chem.* **2011**, 184, 2854.
- [121] B. K. Greve, K. L. Martin, P. L. Lee, P. J. Chupas, K. W. Chapman, A. P. Wilkinson, *J. Am. Chem. Soc.* **2010**, 132, 15496.
- [122] T. Hamada, K. Takenaka, *J. Appl. Phys.* **2011**, 109, 07E309.
- [123] K. Takenaka, H. Takagi, *Appl. Phys. Lett.* **2005**, 87, 261902.
- [124] J. C. Lin, B. S. Wang, S. Lin, P. Tong, W. J. Lu, L. Zhang, W. H. Song, Y. P. Sun, *J. Appl. Phys.* **2012**, 111, 043905.
- [125] R. Huang, L. Li, F. Cai, X. Xu, L. Qian, *Appl. Phys. Lett.* **2008**, 93, 081902.
- [126] K. Takenaka, K. Asano, M. Misawa, H. Takagi, *Appl. Phys. Lett.* **2008**, 92, 011927.
- [127] B. Y. Qu, B. C. Pan, *J. Appl. Phys.* **2010**, 108, 113920.

- [128] P. Tong, D. Louca, G. King, A. Llobet, J. C. Lin, Y. P. Sun, *Appl. Phys. Lett.* **2013**, *102*, 041908.
- [129] C. Wang, L. Chu, Q. Yao, Y. Sun, M. Wu, L. Ding, J. Yan, Y. Na, W. Tang, G. Li, Q. Huang, J. W. Lynn, *Phys. Rev. B* **2012**, *85*, 220103(R).
- [130] Y. Sun, C. Wang, Y. Wen, L. Chu, H. Pan, M. Niez, *J. Am. Ceram. Soc.* **2010**, *93*, 2178.
- [131] K. Takenaka, T. Hamada, D. Kasugai, N. Sugimoto, *J. Appl. Phys.* **2012**, *112*, 083517.
- [132] Z. Chen, R. Huang, X. Chu, Z. Wu, Z. Liu, Y. Zhou, L. Li, *Cryogenics* **2012**, *52*, 629.
- [133] Y. Wang, T. Wen, C. Park, C. Kenney-Benson, M. Pravica, W. Yang, Y. Zhao, *J. Appl. Phys.* **2016**, *119*, 025901.
- [134] X. Song, Z. Sun, Q. Huang, M. Rettenmayr, X. Liu, M. Seyring, G. Li, G. Rao, F. Yin, *Adv. Mater.* **2011**, *23*, 4690.
- [135] H. Luo, J. Liu, X. Zheng, L. Han, K. Ren, X. Yu, *J. Mater. Chem.* **2012**, *22*, 15887.
- [136] Z. Ci, M. Que, Y. Shi, G. Zhu, Y. Wang, *Inorg. Chem.* **2014**, *53*, 2195.
- [137] L. Chen, A. Luo, Y. Jiang, F. Liu, X. Deng, S. Xue, X. Chen, Y. Zhang, *Mater. Lett.* **2013**, *106*, 428.
- [138] J. K. Park, C. H. Kim, S. H. Park, H. D. Park, S. Y. Choi, *Appl. Phys. Lett.* **2004**, *84*, 1647.
- [139] J. K. Park, K. J. Choi, J. H. Yeon, S. J. Lee, C. H. Kim, *Appl. Phys. Lett.* **2006**, *88*, 043511.
- [140] J. S. Lee, S. Unithratil, W. B. Im, *J. Alloys Compd.* **2013**, *555*, 297.
- [141] S. Park, T. Vogt, *J. Am. Chem. Soc.* **2010**, *132*, 4516.
- [142] W.-C. Lee, S. Park, *Mater. Lett.* **2012**, *79*, 152.
- [143] R. Green, T. Vogt, *J. Solid State Chem.* **2012**, *194*, 375.
- [144] X. Zheng, H. Luo, J. Liu, P. Liu, X. Yu, *J. Mater. Chem. C* **2013**, *1*, 7598.
- [145] A. Akella, D. A. Keszler, *Chem. Mater.* **1995**, *7*, 1299.
- [146] M. Jiao, Y. Jia, W. Lu, W. Lv, Q. Zhao, B. Shao, H. You, *J. Mater. Chem. C* **2014**, *2*, 4304.
- [147] C.-H. Huang, Y.-C. Chen, T.-W. Kuo, T.-M. Chen, *J. Lumin.* **2011**, *131*, 1346.
- [148] M. Xie, L. Zeng, X. Zhou, F. Xie, *Solid State Sci.* **2015**, *39*, 6.
- [149] M. Yamaga, Y. Masui, N. U. Kodama, *Opt. Mater.* **2014**, *36*, 1776.
- [150] K. Dong, J. Liao, S. Xiao, X. Yang, J. W. Ding, *J. Mater. Res.* **2012**, *27*, 2535.
- [151] X. Sun, J. Zhang, X. Zhang, Y. Luo, Z. Hao, X.-J. Wang, *J. Appl. Phys.* **2009**, *105*, 013501.
- [152] X. Xu, X. Yu, D. Zhou, J. Qiu, *J. Solid State Chem.* **2013**, *206*, 66.
- [153] Y. Li, B. Li, C. Ni, S. Yuan, J. Wang, Q. Tang, Q. Su, *Chem.-Asian J.* **2014**, *9*, 494.
- [154] W. B. Im, S. Brinkley, J. Hu, A. Mikhailovsky, S. P. DenBaars, R. Seshadri, *Chem. Mater.* **2010**, *22*, 2842.
- [155] J. A. Kechele, C. Schmolke, S. Lupart, W. Schnick, *Z. Anorg. Allg. Chem.* **2010**, *636*, 176.
- [156] W. Xia, A. Mahmood, Z. Liang, R. Zou, S. Guo, *Angew. Chem., Int. Ed.* **2016**, *55*, 2650.
- [157] D. D. Vaughn II, J. Araujo, P. Meduri, J. F. Callejas, M. A. Hickner, R. E. Schaak, *Chem. Mater.* **2014**, *26*, 6226.
- [158] A. Kong, Q. Lin, C. Mao, X. Bu, P. Feng, *Chem. Commun.* **2014**, *50*, 15619.
- [159] Y. Yuan, L. Yang, B. He, E. Pervaiz, Z. Shao, M. Yang, *Nanoscale* **2017**, *9*, 6259.
- [160] X. Jia, Y. Zhao, G. Chen, L. Shang, R. Shi, X. Kang, G. I. N. Waterhouse, L.-Z. Wu, C.-H. Tung, T. Zhang, *Adv. Energy Mater.* **2016**, *6*, 1502585.
- [161] S. Zhao, M. Li, M. Han, D. Xu, J. Yang, Y. Lin, N.-E. Shi, Y. Lu, R. Yang, B. Liu, Z. Dai, J. Bao, *Adv. Funct. Mater.* **2018**, *28*, 1706018.
- [162] Y. Gu, S. Chen, J. Ren, Y. A. Jia, C. Chen, S. Komarneni, D. Yang, X. Yao, *ACS Nano* **2018**, *12*, 245.
- [163] Z. Cui, G. Fu, Y. Li, J. B. Goodenough, *Angew. Chem., Int. Ed.* **2017**, *56*, 9901.
- [164] Q. Wang, L. Shang, R. Shi, X. Zhang, G. I. N. Waterhouse, L.-Z. Wu, C.-H. Tung, T. Zhang, *Nano Energy* **2017**, *40*, 382.
- [165] M. Zhao, H.-J. Peng, Z.-W. Zhang, B.-Q. Li, X. Chen, J. Xie, X. Chen, J.-Y. Wei, Q. Zhang, J.-Q. Huang, *Angew. Chem., Int. Ed.* **2019**, *58*, 3779.
- [166] H. B. Yang, S.-F. Hung, S. Liu, K. Yuan, S. Miao, L. Zhang, X. Huang, H.-Y. Wang, W. Cai, R. Chen, J. Gao, X. Yang, W. Chen, Y. Huang, H. M. Chen, C. M. Li, T. Zhang, B. Liu, *Nat. Energy* **2018**, *3*, 140.
- [167] B. H. R. Suryanto, H.-L. Du, D. Wang, J. Chen, A. N. Simonov, D. R. MacFarlane, *Nat. Catal.* **2019**, *2*, 290.
- [168] T. Hamada, K. Takenaka, *J. Appl. Phys.* **2012**, *111*, 07A904.
- [169] T. Shimizu, T. Shibayama, K. Asano, K. Takenaka, *J. Appl. Phys.* **2012**, *111*, 07A903.
- [170] K. Takenaka, T. Hamada, T. Shibayama, K. Asano, *J. Alloys Compd.* **2013**, *577*, S291.
- [171] Y. Sun, X.-Q. Chen, S. Yunoki, D. Li, Y. Li, *Phys. Rev. Lett.* **2010**, *105*, 216406.
- [172] L. Ding, C. Wang, L. Chu, J. Yan, Y. Na, Q. Huang, X. Chen, *Appl. Phys. Lett.* **2011**, *99*, 251905.
- [173] Z. Wei, W.-Q. Liao, Y.-Y. Tang, P.-F. Li, P.-P. Li, H. Cai, R.-G. Xiong, *J. Am. Chem. Soc.* **2018**, *140*, 8110.
- [174] Z.-X. Wang, Y. Zhang, Y.-Y. Tang, P.-F. Li, R.-G. Xiong, *J. Am. Chem. Soc.* **2019**, *141*, 4372.
- [175] K. Shi, Y. Sun, J. Yan, S. Deng, L. Wang, H. Wu, P. Hu, H. Lu, M. I. Malik, Q. Huang, C. Wang, *Adv. Mater.* **2016**, *28*, 3761.
- [176] J. Zemen, Z. GerCSI, K. G. Sandeman, *Phys. Rev. B* **2017**, *96*, 024451.
- [177] D. Boldrin, A. P. Mihai, B. Zou, J. Zemen, R. Thompson, E. Ware, B. V. Neamtu, L. Ghivelder, B. Esser, D. W. McComb, P. Petrov, L. F. Cohen, *ACS Appl. Mater. Interfaces* **2018**, *10*, 18863.
- [178] D. Boldrin, E. Mendive-Tapia, J. Zemen, J. B. Staunton, T. Hansen, A. Aznar, J.-L. Tamarit, M. Barrio, P. Lloveras, J. Kim, X. Moya, L. F. Cohen, *Phys. Rev. X* **2018**, *8*, 041035.
- [179] R. E. Schaak, T. E. Mallouk, *Chem. Mater.* **2002**, *14*, 1455.
- [180] K. G. S. Ranmohotti, E. Josepha, J. Choi, J. Zhang, J. B. Wiley, *Adv. Mater.* **2011**, *23*, 442.